Do standing trees affect landslide mobility on forested hillslopes in Japan?

Abstract

Landslide mobility likely changes in response to the effects of standing trees on the landslide runout. However, the properties of standing trees that influence landslide runout are not well understood. In this study, the relationships between the properties of landslides and the heights of standing trees and the runout distances of rainfall-induced landslides (primarily 10^1–10^3 m^3 in volume) in the Hiroshima Prefecture, Japan, were examined to investigate whether the heights of the trees around the runout area change the landslide mobility. The results indicate that the landslide runout was constrained not only by the landslide area and volume but also by the tree height around the runout area. Tall but sparse standing trees did not prevent landslide runout, whereas dense standing trees resulted in relatively low landslide mobility, irrespective of whether the trees were broadleaf or coniferous. A comparison between our landslide inventory and previously reported landslides showed that the landslide mobility was lower in areas with standing trees than in areas without standing trees, such as under experimental conditions and for landslides in Martian and submarine

environments. Therefore, differences in the heights of the trees around the runout area can result in variations in the extent of landslide-related hazards and disturbances.

Keywords: Standing tree; Shallow landslides; Landslide runout; Landslide mobility; Debris flow

1. Introduction

Landslides are hazardous geomorphic processes in mountainous areas that erode hillslopes and often cause damage to residential areas and injury or even death (e.g., Petley, 2012; Dowling and Santi, 2014). Landslide runout entrains channel deposits, erodes channel banks, and transitions into debris flows, thereby distributing sediment across different-sized areas, from the scale of the headwater channels to that of the watershed (e.g., Berger et al., 2011; Bracken et al., 2015; Fan et al., 2019a). The resulting increase in unconsolidated sediment influences the sediment regime and changes the landscape through subsequent sediment transport and deposition processes that are primarily driven by fluctuations in the stream power (e.g., Korup, 2005; Bennett et al., 2014; Broeckx et al., 2020; Campforts et al., 2020). Therefore, it is important to have information concerning the characteristics of the landslide runout to support the mitigation of disasters and to understand the sediment dynamics.

Landslide runout is characterized by relationships between the vertical drop (fallen) height (H) to the runout distance (L), where H indicates the elevation distance from the top of the landslide scar (the release point) to the lower end of the sediment deposition area (the landslide termination point) and L indicates the

projected horizontal distance from the top of the landslide scar to the lower end of the deposition area (e.g., Legros, 2002; Lucas et al., 2014). The *H* to *L* ratio is called the apparent friction coefficient (e.g., Dade and Huppert, 1998; Legros, 2002; Lucas et al., 2014), whereas the *L* to *H* ratio is called the landslide mobility (Pudasaini and Miller, 2013; Baselt et al., 2022). The relationship between *H* and *L* demonstrates that the runout distance is increasingly dependent on the landslide volume when landslides exceed a threshold volume range (>10^5–10^7 m^3) irrespective of differences in the environmental settings, such as terrestrial and Martian surfaces and submerged slopes (Pudasaini and Miller, 2013). Therefore, the physical friction-related processes that govern the landslide mobility have been widely recognized as a major constraint on the runout distances of landslides (e.g., Pudasaini and Miller, 2013; Lucas et al., 2014).

While this information holds for large landslides, there is still discussion concerning what controls the mobility of smaller landslides (<~10^5 m^3). Debris flows formed by landslides entrain sediment and trees around the runout area as they descend (e.g., Johnson et al., 2000; Miller et al., 2003; Wohl et al., 2009; Ruiz-Villanueva et al., 2014, 2016; Piton and Recking, 2016; Swanson et al., 2021; Tsunetaka et al., 2021). Entrained trees are broken into pieces, which

potentially change the flow regime of the debris flows, depending on their size and composition ratio (e.g., Jackson and Sturm 2002; Benda et al., 2003; May and Gresswell, 2003a). Debris flows that form from small landslides may be several meters in depth; therefore, the ratio of the entrained tree pieces can be relatively high and cannot be ignored. This means that standing trees in the runout area may have a greater influence on the runout characteristics of small landslides than large landslides.

Relatively large tree pieces, namely those >0.1 m in diameter and >1 m in length (Jackson and Sturm 2002; Tang et al. 2018), which are referred to as large wood (LW), can be entrapped as logjam in a channel (e.g., Ruiz-Villanueva et al., 2016). A logjam consisting of LW behaves as an obstacle that prevents the descent of debris flows, potentially leading to local sediment deposition and preventing flow runout (e.g., May, 2002; May and Gresswell, 2003b; Benda et al., 2003; Lancaster et al., 2003). While LW may decrease the runout distance, small tree pieces may increase the fluidity of debris flows via their slurry-like behaviour in the pore fluid, which can facilitate a more distal runout of the sediment (Tang et al., 2018). Moreover, if dense standing trees in the channel are not eroded by the landslide, their bases and roots can serve as obstacles that alter the

superficial channel geometry and directly prevent the sediment runout (Booth et al., 2020). Therefore, how trees around the runout area influence the mobility of landslide-generated debris flows in response to their properties is not well understood.

The primary objective of this study is to examine whether differences in tree heights around the runout area change the landslide mobility. A heavy rainfall event in July 2018 in the Hiroshima Prefecture, Japan, triggered numerous landslides and provided a test field that allowed us to compare the runout distances of landslides with respect to the heights of the standing trees. We propose new indices that evaluate the properties of the heights of the standing trees around the runout areas of the landslides using digital elevation models (DEMs) and digital surface models (DSMs) from before and after the landslides. We then investigate the relationship between the landslide runout distance and the tree height. Our final objective is to determine the extent to which standing trees constrain the landslide mobility in comparison with other landslide properties.

2. Study site

We analysed the landslides that occurred in the Hiroshima Prefecture, Western Japan, in July 2018 (Figure 1a). The Hiroshima Prefecture has a vulnerable lithology comprising weathered granite, such that this region has repeatedly experienced severe sediment disasters resulting from landslides and debris flows. The July 2018 landslide event was one of the most severe disasters in the area with respect to the size and number of landslides that occurred (Kaibori et al., 2018).

A stationary front associated with Typhoon Prapiroon produced over 400 mm of precipitation from July 5 to July 7, 2018, which triggered over 8,000 landslides in the Hiroshima Prefecture (Tsunetaka, 2021). The landslides occurred on forested hillslopes at elevations of between approximately 30 m and 250 m (Tsunetaka, 2021). The hillslopes were mostly covered with broadleaf or coniferous forests and included trees with different heights. This landslide event therefore provided an opportunity to investigate how differences in the tree height around the runout area impacted the landslide mobility.

To support our investigation of the July 2018 landslide event, we obtained airborne laser scanning (ALS) data from October 2018, which provided DEMs and DSMs covering most of the Hiroshima Prefecture. We also obtained DEMs

and DSMs acquired by ALS in February 2015 of comparable quality over part of the Hiroshima Prefecture (Figure 1b). We then analysed the landslides that occurred in this area in July 2018 using the DEMs and DSMs from before and after the landslide event.

3. Methods

We compared how the landslide characteristics and the heights of the standing trees around the runout area influenced the landslide mobility. To accomplish this, we assembled an inventory of information concerning the landslide and runout areas. We then analysed the size properties of the landslides using the landslide inventory. We developed new indices to evaluate the geometry of the standing trees around the runout area and investigated whether the standing trees influenced the landslide mobility in comparison with the other landslide properties.

3.1. Landslide inventory

To compare the landslide properties and the runout characteristics, we used a landslide inventory compiled from an investigation organized by the

Forestry Agency (Forestry Agency, 2019). When landslides, particularly small landslides (<10^1–10^2 m^2), are mapped from aerial images, uncertainties are inevitable and errors arise from differences in the scale, date, and quality of the data sources and the expertise of the interpreters (Malamud et al., 2004). Despite these shortcomings, aerial images are still recognized as a reliable tool for mapping landslides (e.g., Carrara et al., 1992; Guzzetti et al., 2012). Landslides triggered in the Hiroshima Prefecture in 2018 were therefore manually mapped from DEMs and orthophotos acquired by ALS in October 2018 (Forestry Agency, 2019).

As the first step of the landslide mapping, areas of bare land on hillslopes were tentatively mapped as outlines of landslide scars from orthophotos (0.25-m resolution) acquired by ALS in October 2018. Using the DEM (1-m resolution) acquired by ALS in October 2018, contours at 1-m intervals and surface slopes were calculated. The landslide scars, contours, surface slopes, and edges of each landslide scar mapped from the orthophotos were overlain, accurately realigned, and mapped again as polygon data. The resulting landslide polygons with the scar outlines were compared with earlier satellite and aerial images to ascertain whether the corresponding landslides were triggered by the rainfall

event in July 2018. Using this comparison, only landslides that occurred in July 2018 were retained in the inventory and earlier landslides were excluded from the analysis.

We investigated the types of forest on the landslide scars using the results of a vegetation survey from the Biodiversity Center of Japan (Biodiversity Center of Japan, 2021). The vegetation types of the landslide scars were categorized into three groups: deciduous and evergreen broadleaf forests were defined as *broadleaf forests*; forests consisting of deciduous and evergreen conifers were defined as *coniferous forests*; and other vegetation, such as orchards, bamboo forests, and grassland, were defined as *others*. We assumed that the vegetation on the landslide scar was analogous to that of the corresponding runout area.

3.2 Landslide properties

We investigated the landslide volume–area (V–A) scaling relationship (e.g., Guzzetti et al., 2009; Larsen et al., 2010) and the frequency–area distribution (FAD; e.g., Malamud et al., 2004; Tanyaş et al., 2019) to assess the relevance of the size of the landslide area to the volume and frequency of the

landslides.

The *V*–*A* scaling relationship is described by a power law:

$$V = \alpha A^{\gamma} \qquad (1),$$

where α is the interception parameter, which likely has no physical meaning, and γ is the scaling parameter, which determines the increase in the landslide volume with increasing landslide area (e.g., Larsen et al., 2010).

The volume of each landslide area was calculated using the DEMs from before and after the landslide event. First, the DEM of the differences (DoD) was calculated by subtracting the DEM measured in 2015 (before the event) from the DEM measured in 2018 (after the event). Because the resolutions of the DEMs from both before and after the landslide event were 1 m in grid size, the resolution of the DoD was also set to 1 m. Next, the volumetric differences were calculated with respect to each landslide scar using Eq. (2), similar to Staley et al. (2014):

$$V = \frac{A \times \sum_{(i,j)=1}^{n} \Delta Z_{(i,j)}}{n} \qquad (2),$$

where $\Delta Z_{(i,j)}$ is the elevation difference calculated by the DoD at each grid (*i*, *j*; given the coordinates of each grid in meters) and *n* is the total number of grids in the area *A* (Staley et al., 2014).

We investigated the scaling parameters in Eq. (1) by plotting the *V*–*A*

relationships on the log–log *V*–*A* plane. On the basis of the landslide inventory, we calculated the area of each landslide scar and derived the FAD of the analysed landslides. The cut-off point (the lower limit of the landslide area that met the power-law scaling of the FAD) was derived (e.g., Tanyaş et al., 2019; Marc et al., 2019) using the methodology of Clauset et al. (2009). Moreover, the average tree height of each landslide scar prior to the 2018 landslide event was measured via the difference between the DEM and the DSM measured in 2015. The area, volume, and average tree height were compared with the corresponding runout distance to investigate whether the landslide properties constrained the runout characteristics.

3.3 Landslide runout

To measure the runout distances using the landslide inventory, the corresponding runout area was mapped as line data based on the DEM and orthophotos measured in 2018. Because most of the debris flows generated by the landslides reached the high-order channel streams, it was not possible to accurately define the lower end of the sediment deposition area in many cases. Note that, the drop height (*H*) and the runout distance (*L*) are generally defined

as the projected vertical and horizontal distances, respectively, from the top of the landslide scar to the lower end of the sediment deposition area (Figure 2a). The difficulty of mapping the lower end of the sediment deposition area made it impossible to measure *H* and *L* for all the landslides in the inventory. To remedy this issue and still meet the required mapping consistency, the runout area was defined as the area between the lower edge of the landslide scar and the upper end of the deposition area (Figure 2b). The runout distance and the drop height used in this study (*L′* and *H′*) were defined as the sum of the projected horizontal distances and the elevation difference, respectively, between the landslide scar and the runout area (Figure 2b). Considering that both *L* and *H* can usually be measured with a relative error of less than 20% (Legros, 2002), we assumed that the errors of the *L′* and *H′* measurements had the same tolerance.

Several landslides sometimes occurred in a single sub-watershed, and therefore, the generated debris flows sometimes descended in the main channel stream as a confluent flow. In such cases, we could not define a runout area for the individual landslides; therefore, we excluded such confluent flows from the landslide inventory. Landslides with runout affected by check dams are likely to have smaller runout distances, which prevents the investigation of whether

standing trees can alter landslide mobility. We therefore also excluded landslides with runout stopped by check dams in the upper reach from the landslide inventory. Following this screening, a total of 366 landslides were retained in the inventory and were therefore analysed in this study.

The sizes of the standing trees are likely related to both the relatively long- and short-runout characteristics of landslides in response to the extent of erosion and entrainment linked to trees. To investigate how the tree properties of each landslide contributed to either the long- or short-runout characteristics, we tentatively categorized the landslides into two groups based on the average value (115.0 m) of L' for the landslide inventory (Figure 3): landslides with $L' > 115.0$ m were categorized as long-runout landslides, whereas landslides with $L' \leq 115.0$ m were categorized as short-runout landslides. The long- and short-runout landslides accounted for ~25% and ~75% of the landslide inventory, respectively.

3.4 Analysis

3.4.1 Analysing the heights of the standing trees using swath profiles

The swath profiles around the runout areas were calculated to support an analysis of the impacts of the heights of standing trees on the landslide mobility.

A swath profile describes the average properties of the area surrounding a single base profile (e.g., the red line in Figure 4a) and is generally used to investigate the asymmetry of properties along a base profile of topography and precipitation, among others (e.g., Hergarten et al., 2014; Hergarten and Robl, 2021). We attempted to obtain a proxy of the heights of the standing trees around the runout areas using a swath-profile-based approach. Other methods have been used to investigate tree heights elsewhere, such as the tree-crown method (Sankey et al., 2013; Zhen et al., 2015); however, there may be issues with data quality when using the tree-crown approach and this method is not appropriate for the complex tree-crown shapes that are common in mixed broadleaf forests. Conversely, swath profiles can encapsulate information concerning the tree height regardless of variations in the crown shape, potentially providing a promising basis for comparison.

For the tree-height analysis, we obtained crown-height models (CHMs) from before and after the 2018 landslide event. The CHM from before the landslide event was calculated by subtracting the DEM from the DSM with respect to the ALS in February 2015, whereas the CHM from after the landslide event was calculated by subtracting the DEM from the DSM with respect to the ALS in

October 2018. Similar to the DEMs and DSMs, the resolution of the CHMs both before and after the landslide event was set to 1 m. On the CHM from before the landslide event, the swath profiles around the runout areas show geometric features mostly consisting of standing trees. Therefore, for example, when the minimum values of the swath profile were relatively high, we can say that there was very little quasi-bare land and that the runout area had a dense coverage of standing trees before the landslide runout. Conversely, low minimum values on the CHM from after the landslide event indicate that the landslide runout entrained sediment and trees and caused substantial channel and bank erosion.

We followed the methodology of Hergarten et al. (2014) and used CHMs with a spatial resolution of 1 m from before and after the landslide event to calculate the swath profiles along each line of the mapped runout areas (Figure 4). We maintained a width of 30 m for the swath profile to ensure that we could investigate the entire area affected by bank erosion (Figure 4a). The average minimum (TH_{min}), mean (TH_{mean}), and maximum (TH_{max}) values of the swath profile were used as indices of the tree height (TH) (Figure 4b). These parameters were compared with the landslide runout distance to investigate whether the tree-height properties had any effect on the landslide mobility.

3.4.2 Statistical analysis

To investigate whether the standing-tree properties significantly affect the landslide mobility, we conducted a statistical analysis. First, differences in the examined landslide properties (area, volume, and average tree height of each landslide scar) and tree-height properties (TH_{min}, TH_{mean}, and TH_{max} from before and after the landslide event) were statistically compared using a nonparametric test. We performed the Wilcoxon–Mann–Whitney (MW) test for the two landslide groups with respect to the landslide runout (i.e., long- and short-runout landslides). The null hypothesis was that the examined property had been fitted between two groups; therefore, a calculated p-value of <0.05 indicated that the examined property significantly differed between the long- and short-runout landslides.

To assess which property governed the landslide mobility, we performed a principal component analysis (PCA) for the same parameters as used for the MW test (i.e., the area, volume, and average tree height of each landslide scar, as well as TH_{min}, TH_{mean}, and TH_{max} from before and after the landslide event). On the basis of this analysis, we inferred the contributions of the analysed landslide and the tree-height properties to the changes in the landslide runout to

determine whether standing trees can constrain the landslide mobility. Both the MW test and the PCA were performed using R (R Core Team, 2022).

3.4.3 Landslide mobility

To investigate whether the data in the present study characterize trends in landslide mobility compared with other datasets that represent standing trees under various environmental conditions, we examined previously reported landslide mobility data (Baselt et al., 2022 and references therein). First, following Pudasaini and Miller (2013), the landslide mobility was defined as the ratio of the runout distance (L') to the drop height (H'). Both L' and H' are smaller than the corresponding L and H values (Figure 2). Because the deposition areas have mostly gentle slopes compared with the landslide scars (e.g., Figure 2), the difference between H' and H is relatively small compared with the difference between L' and L, which may mean that the landslide mobility was underestimated.

To quantitatively investigate the underestimation extent of the landslide mobility owing to the use of L' and H', we compare L' and L as well as H' and H with respect to landslides for which both L and H values are available. In the

examined landslide inventory, we measured *L* and *H* values with respect to 29 landslides, using the DEMs and orthophotos measured in 2015 and 2018. In the subset consisting of these 29 landslides, the *L* values were greater than those of the corresponding *L′* (see Supporting Information, Figure S1). The differences between *L* and *L′* slightly increased with increasing runout distance. Similarly, the *H* values were greater than those of the corresponding *H′* (Figure S2). The slopes of the linear regression curves between *L* and *L′* and between *H* and *H′* were close to 1, but their intercept values differed at 12.9 and 3.10, respectively (Figures S2 and S3). This indicates that the differences between *L* and *L′* were greater than those between *H* for *H′*. Consequently, the landslide mobility using *L′* and *H′* (i.e., *L′*/*H′*) was potentially underestimated by approximately 10%–20% (maximum ~ 30%) in comparison with the corresponding *L*/*H* (Figure S3). While considering this potential bias in the landslide mobility, we compared our dataset with the landslide mobility measured for terrestrial, experimental, submarine, and Martian landslides (Baselt et al., 2022 and references therein).

4. Results

4.1 Landslide scaling characteristics

The landslide area ranged between approximately 10^1 m^2 and 10^3 m^2 (Figure 5). The *V–A* scaling relationship of the landslide event resulted in a value of close to 1 for the scaling parameter (γ) (Figure 5), which is low compared with previously reported values (e.g., Larsen et al. (2010) reported γ values of approximately 1.1–1.3 for shallow, soil-based landslides). Most plots were distributed along the line for a mean depth of 1 m regardless of the ranges of the landslide areas and volumes. Therefore, a γ value of close to 1 indicates that the landslide volume monotonically increases as the landslide area increases. Indeed, the interquartile range of the landslide depth varied somewhat between approximately 0.8 m and 1.5 m and had a median of ~1.2 m (Figure 6a). The median of the surface slope at the landslide scar was approximately 35–38° and was similar before and after the event (Figure 6b), which indicates that most of the landslide scars corresponded to the slipping of a soil layer with a uniform depth of approximately 1 m.

The FAD for the landslide event indicated that the landslides with areas of over 174 m^2 conformed to the power-law scaling and that the smaller landslides had a different frequency trend characterized by the rollover point (the inflection point of the frequency) (Figure 7). Both the power-law fitting and the rollover point

for the FAD are quintessential trends of landslide inventory maps (e.g., Malamud et al., 2004; Tanyaş et al., 2019). The FAD indicated that the frequency of landslides with areas on the order of ~10^2 m^2 steeply increases and that there are a small number of landslides with areas greater than 10^3 m^2. Overall, landslides with a depth of ~1 m and an area of ~10^2 m^2 accounted for a significant component of the examined landslides.

4.2 Factors constraining the landslide runout distance

The average tree heights at the landslide scar before the event varied considerably, between 0 m and 20 m, and were not correlated with the landslide area or volume (Figure 8). Conversely, the landslide area and volume were somewhat correlated with the runout distance (Figure 9). The power-law fittings indicated that the runout distance increased with increasing landslide area and volume. However, the values of the coefficient of determination for the landslide area and volume were 0.33 and 0.18, respectively, indicating that properties related to the landslide size somewhat constrained the runout distance but alone could not completely explain the extent of the landslide runout.

Different factors constrain the landslide runout, and therefore the height

of the standing trees around the runout area may have influenced the runout distance. Both before and after the landslide event, the runout distance (L') increased as the value of TH_{min} decreased (Figures 10a and b). Focusing on the long-runout landslides (i.e., $L' > 115.0$ m), with two exceptions, the values of TH_{min} were <5 m and were mostly <2.5 m. The TH_{min} values from after the event were much smaller than those from before the event, especially for the long-runout landslides. When TH_{min} was over 5 m, the runout distance was relatively low and ranged from approximately 16 m to 150 m, regardless of the type of forest.

The TH_{mean} values of the short-runout landslides (i.e., $L' \leq 115.0$ m) widely ranged from ~0 m to 18 m both before and after the landslide event (Figures 10c and d). Unlike the wide-ranging values of the short-runout landslides, the TH_{mean} values of the long-runout landslides were mostly in a narrow range from ~2.5 m to 10 m, especially for landslides with L' values of >400 m, which indicates that the long-runout landslides exhibited higher and lower TH_{mean} values compared with the lower and upper limits, respectively, of the TH_{mean} values for the short-runout landslides. Given this, the relationships between the TH_{mean} values and the runout distance were not clear in comparison with those of the TH_{min} values (Figures 10a–d).

The relationships between TH_{max} and the runout distance exhibited an inverse trend in comparison with those between TH_{min} and the runout distance (Figures 10e and f). As TH_{max} increased, the runout distances of the landslides also tended to increase both before and after the event regardless of the forest type. Focusing on the long-runout landslides, the TH_{max} values were mostly >5 m, whereas TH_{max} values of <5 m were observed for the short-runout landslides. However, this trend in TH_{max} was somewhat unclear compared with the trend in TH_{min} and the runout distances varied considerably, especially when TH_{max} exceeded ~10 m (Figure 10).

4.3 Statistical comparison of the landslide and tree-height properties

The MW tests revealed significant differences in the landslide and tree-height properties between the long- and short-runout landslides (Figure 11). The landslide area and volume of the long-runout landslides tended to be greater than those of the short-runout landslides, with a *p*-value of <0.0001, indicating the significance of this difference (Figures 11a and b). This trend is consistent with the relationships between the runout distance and the landslide area and volume (Figure 9). Similarly, the values of the average tree height of the landslide scar of

the long-runout landslides were greater than those of the short-runout landslides (Figure 11c). The *p*-value was 0.0038 (i.e., <0.05), which indicates the significance of the differences; however, this *p*-value was relatively large in comparison with those of other properties (Figure 11).

The MW tests with respect to the *TH* indices statistically supported the relevance of the tree-height properties and landslide-runout characteristics. The *p*-values of <0.05 indicate that the TH_{min} values of the long-runout landslides were significantly smaller than those of the short-runout landslides both before and after the landslide event (Figures 11d and e). The boxplots indicate that the interquartile ranges of the TH_{min} values considerably differed between the long- and short-runout landslides, especially after the landslide event; this is reflected in the differences in the *p*-values before the event (0.0046) and after the event (<0.0001). The *p*-value of TH_{min} before the event was the highest of the examined properties (Figure 11). After the event, the TH_{min} values of the long-runout landslides were mostly less than ~1 m (Figure 11e).

Conversely, the boxplots with respect to the TH_{mean} indices revealed that the TH_{mean} values of the long-runout landslides were larger than those of the short-runout landslides both before and after the landslide event, with the *p*-

values indicating the significance of these differences (Figures 11f and g). The differences in the boxplots with respect to TH_{max} were more distinct with respect to the extent of the landslide runout (Figures 11h and i). The interquartile ranges of TH_{max} did not overlap for the long- and short-runout landslides; this is a remarkable characteristic that was observed only for TH_{max}. Overall, all examined properties, excluding TH_{min}, indicated that larger values were related to relatively long runout distances. Conversely, increasing the TH_{min} value was related to reducing the runout distance.

The PCA results provide information on how the respective properties constrain the runout distance. The PC1 score (i.e., *x*-axis) explained 51% of the data variance and primarily evaluated the loadings with respect to the TH_{mean} and TH_{max} indices before and after the landslide event, and the average tree height of the landslide scar (Figure 12). The relatively short arrow of the average tree height (i.e., the green arrow indicating Tree in Figure 12) indicated a relatively low loading with respect to the landslide runout, which is consistent with the relatively low *p*-value of the MW test (Figure 11c). In this sense, the PC1 scores support the relevance of higher tree height with regard to longer landslide runout.

The PC2 score explained 20% of the data variance; therefore, the PC1

and PC2 scores together explained 71% of the data variance (Figure 12). The landslide area and volume contributed to the loading for the PC2 score. Indeed, plots indicating the long-runout landslides were mostly distributed below a PC2 score of <0. Importantly, the TH_{min} values acted as loadings that influenced PC2 in the inverse direction in comparison with the landslide area and volume. This corresponds to the observation that high TH_{min} values reduced the runout distance (Figures 10a and b), as well as the observation that only the TH_{min} values of the long-runout landslides were smaller than those of the short-runout landslides (Figures 11d and e). The PC2 scores indicate that the TH_{min} index captures the tree properties that reduced the landslide mobility.

In this context, the relationships between the TH_{min} and TH_{max} indices differed in response to the runout distance. Even though the data variance was considerable, the TH_{min} values were more or less correlated with the TH_{max} values before the landslide event (Figure 13a). The TH_{min} values of the long-runout landslides were relatively low in comparison with short-runout landslides with similar TH_{max} values. After the landslide event, the data variance of the relationships between the TH_{min} and TH_{max} indices for both long- and short-runout landslides became more considerable (R^2 < 0.3), primarily because of the

increase in the number of data points with TH_{min} values of approximately zero (Figure 13b). However, even after the landslide event, the TH_{min} values of the short-runout landslides tended to be larger than those of long-runout landslides with similar TH_{max} values.

4.4 Variation in landslide mobility

On the basis of the results that TH_{min} was related to the decrease in the runout distance (Figures 11 and 12) and that both of the long- and short-runout landslides exhibited TH_{min} values of ≥5 m before the landslide event, the landslide inventory was grouped into two types: landslides with TH_{min} values before the landslide event of ≥5 m and landslides with TH_{min} values before the event of <5 m. In this study (our landslide inventory), the runout distance (L') and the drop height (H') ranged from approximately 10 m to 900 m and from 5 m to 260 m, respectively (Figure 14). These data were distributed in the data gap between the experimental landslides (upward triangle symbols) and the natural landslides (cross symbols). On the log–log plane, the runout distance (L') increased as the drop height (H') increased, which is similar to previous findings for surface terrestrial, Martian, submarine, and experimental landslides (e.g., Pudasaini and

Miller, 2013). The landslide mobility (i.e., L'/H') in this study ranged from approximately 1 to 10, which is within the typical mobility of landslides observed elsewhere; for example, Baselt et al. (2022) reported L/H values of between 1 and 35. Landslides with TH_{min} values of ≥5 m before the event mostly plotted above the line at which L/H = 5. Therefore, high values of TH_{min} were linked to low landslide mobility.

Focusing on landslides with volumes of >10^5 m^3, the mobility of such landslides tended to increase with increasing landslide volume (Figure 15). However, the relevancy of the landslide mobility to the landslide volume in this study was not clear in comparison with these large landslides; in addition, the mobility of landslides with TH_{min} values of ≥5 m was relatively low irrespective of the landslide volume. Therefore, the changes in the landslide mobility exhibited different trends in response to the ranges of the landslide volume; this highlights the fact that the mobilities of landslides with volumes of <10^5 m^3 were likely constrained not only by the landslide volume but also by the tree heights.

Landslides in experimental, submarine, and Martian settings are not influenced by standing trees, and therefore the lower limit of the mobility of these landslides could be assumed as the lower limit of the landslide mobility without

the influence of trees (Figure 15). The lower limit of the landslide mobility without the influence of trees corresponded to the lower limit of the experimental landslides (L/H = ~1.73); this value is similar to that for Martian landslides (L/H = ~1.79) but the volumes of these landslides differ substantially (~10^{-2} versus 10^{8} m^3). Importantly, some landslides that were possibly affected by standing trees (i.e., landslides elsewhere on Earth and in this study) are below the lower limit of landslide mobility without standing trees. The volumes of such landslides range from ~10^{1} m^3 to 10^{7} m^3, a range that is greater than that of experiments and less than that of Martian landslides. Therefore, the influence of the trees is related to the wide-ranging mobility of the landslides in this study and other previously reported instances on the surface of the Earth.

5. Discussion

5.1 Effects of standing trees in the runout area on landslide mobility

Our results highlight that, for landslides with volumes of less than ~10^{5} m^3, landslide mobility is constrained not only by the landslide properties (i.e., area, volume, and average tree height of the landslide scar) but also by the tree-height properties of the standing trees around the runout area. Relatively high TH_{max}

values lead to an increase in the runout distance (Figures 11h and i), whereas relatively high TH_{min} values reduce the landslide runout (Figures 11d and e). This inverse trend can be interpreted via the differences in the relationships between the TH_{max} and TH_{min} values with respect to the runout distance.

The TH_{max} values are related to the tallest standing trees around the runout area and directly reflect the tree-height properties. In contrast, because the TH_{min} values evaluate the minimum heights, including bare land in which landslides have eroded sediment and trees (i.e., the tree height is zero), the removal of trees by excessive channel and bank erosion is reflected in the decrease in the TH_{min} value. In other words, high TH_{min} values indirectly indicate that the runout area mostly does not contain bare land and is densely covered with standing trees. Indeed, the difference in the internal meaning between the TH_{max} and TH_{min} values is reflected in the difference in the loadings in the PCA analysis (Figure 12). Importantly, even though high TH_{max} values are potentially somewhat related to increases in the runout distance, tall but sparse standing trees (i.e., high TH_{max} and low TH_{min} values) were linked with longer runout distances (Figure 13). Therefore, tall but sparse standing trees likely cannot reduce the runout distance.

In this context, low TH_{min} values, rather than high TH_{max} values, may be closely related to increases in the runout distance. Focusing on tree properties before the landslide event, the short-runout landslides exhibited high TH_{min} values in comparison with long-runout landslides with similar TH_{max} values (Figure 13a). The low TH_{min} values of the long-runout landslides were emphasized after the event, and most of the long-runout landslides after the event exhibited low TH_{min} values close to zero (Figure 13b). These likely resulted from increases in bare land as a result of the erosion of sediment and trees in the runout area, potentially facilitating landslide runout via increases in the momentum of the generated debris flows.

High TH_{min} values indicate that standing trees densely cover the runout area in the form of barriers or baffle arrays of trees, which can block the landslide runout. Such obstacles can cause a runup of debris flow formed by landslides (Iverson et al., 2016; Li et al., 2020). Debris-flow runup decelerates and redirects the flow, thereby reducing the runout distance (Iverson et al., 2016). Because the examined landslides were shallow (~1 m depth) (Figures 5 and 6), the flow depth of the generated debris flows likely ranged on the order of a few meters. Standing trees with high TH_{min} values could therefore behave as such obstacles, causing

debris-flow runup and reducing the runout distance. Taller trees have larger crowns (e.g., Chen et al., 2006), thus leading to a reduced standing tree density owing to self-thinning (e.g., Yoda, 1963; Westoby, 1984; Weller, 1987). In this context, high TH_{max} values are somewhat linked to sparse standing trees that cannot behave as obstacles to cause debris-flow runup. In this sense, the relevance of high TH_{max} and low TH_{min} values to relatively long runout distance (Figure 13) can be interpreted that tall but sparse standing trees cannot behave as obstacles that cause debris-flow runup. This interpretation can explain why only the TH_{min} values were related to the reduced landslide mobility.

The mobilities of landslides with TH_{min} values of ≥5 m were low compared with landslides that occurred in environments without standing trees, namely experimental, submarine, and Martian landslides (Figures 14 and 15). This reflects the prevention of runout by standing trees. Therefore, impact of standing trees on landslide runout cannot be ignored and should be considered along with other agents that change landslide runout characteristics, such as the grain size distribution and sediment composition (Major and Iverson, 1999; De Haas et al., 2015; Hürlimann et al., 2015; Baselt et al., 2022). In contrast, the highest value of the landslide mobility in this study was ~10, which is comparable to or less than

that of other landslide instances (Figure 15). In this sense, the tree-height properties more or less reduced the landslide runout but were not likely responsible for the increase in the landslide mobility, in terms of comparisons between the landslide mobilities in various environmental settings. Therefore, the differences in the landslide mobility in response to the TH_{min} value support the interpretation of an inverse trend between the landslide runout and the TH_{max} or TH_{min} indices.

Some landslides with low TH_{min} values of <5 m exhibited short runout distances of <100 m (Figures 10a and b) and low mobilities of <2 (Figures 14 and 15). This likely indicates that the landslide runout was somewhat prevented not only by standing trees but also by other factors, such as the topography and anthropogenic land use (e.g., paddy fields and farmland). Moreover, as mentioned in subsection 3.3, we did not use the original definition for the runout distance and drop height (L and H) but instead applied L' and H'. The landslide mobility using L' and H' may produce an underestimate (maximum ~ 30%) compared with that using L and H (see Supporting Information, Figure S3). Because the differences between L and L' and those between H and H' do not correlate with the TH_{min} values before the landslide event (Figures S4 and S5),

the estimation with respect to the extent of the underestimation is difficult. However, even considering these effects, by comparing landslides with $TH_{min} \geq 5$ m with those with $TH_{min} < 5$ m, it is clear that at least the TH_{min} variation is linked to mobility differences (Figures 14 and 15).

5.2 Implications for how information concerning standing trees contributes to estimates of sediment dynamics

The proposed *TH* indices can be calculated from the CHM (i.e., the DEM and DSM). It is becoming easier to obtain CHM data at a resolution of less than 1 m as ALS- (e.g., Yun et al., 2021) and UAV-based measurements (e.g., Swayze et al., 2021) are increasingly used. Furthermore, data from satellite-based LiDAR systems are also available (e.g., Potapov et al., 2021). By comparing TH_{min} from different channels using these data, we can investigate channels where there is a potential for sediment disasters and significant disturbances when landslides occur, thereby helping to identify watersheds that should be prioritized for mitigating landslide-related hazards.

Notably, both broadleaf and coniferous forests with high TH_{min} values can prevent landslide runout (Figures 10a and b), which implies that the tree density

and height along a channel constrain the landslide runout regardless of the tree species. Forest succession is driven not only by ecological processes (e.g., Brzeziecki and Kienast, 1994; Barnes and Dibble, 1988) but also by anthropogenic disturbances (e.g., Vilén et al., 2012) and can therefore progress even without landscape changes. Because of this, information concerning how the TH_{min} value has changed over time could be used to support predictions of future changes in the potential amounts of sediment transport relative to tree growth, deforestation, and forestry.

6. Conclusions

In this study, we investigated whether standing trees around landslide runout areas influence the landslide mobility by examining the relationships between the landslide and tree-height properties and the runout distances of rainfall-induced landslides in the Hiroshima Prefecture, Japan. The landslide runout was affected not only by the landslide area and volume but also by the tree heights around the runout area. When tall trees were sparsely retained because of the removal of many standing trees via the erosion of channels and banks, such trees could not prevent the landslide runout. In contrast, standing

trees that densely covered the runout area reduced the runout distance and decreased the landslide mobility. The decrease in the landslide mobility resulting from dense standing trees was remarkable in comparison with other previously reported landslides, especially landslides that occurred in environments without trees (i.e., experimental, submarine, and Martian landslides). These results highlight that variations in the tree height around the runout area are responsible for changes in the extent of landslide-related hazards and sediment dynamics. Our evaluation was based on tree-height indices calculated using DEMs and DSMs. Therefore, if DEMs and DSMs with adequate quality are available, this approach can serve as a basis for discerning channels with a further potential for landslide-related hazards and forest disturbances.

References

Abele G. 1974. Bergstürze in den Alpen: Ihre Verbreitung, Morphologie und Folgeerscheinungen (rockfalls in the Alps: distribution, morphology, and impacts). Wissenschaftliche Alpenvereinshefte 25, München.

Barnes WJ, Dibble E. 1988. The effects of beaver in riverbank forest succession. Canadian Journal of Botany 66: 40-44.

Baselt I, de Oliveira GQ, Fischer JT, Pudasaini SP. 2022. Deposition morphology in large-scale laboratory stony debris flows. Geomorphology 396: 107992.

Benda L, Veldhuisen C, Black J. 2003. Debris flows as agents of morphological heterogeneity at low-order confluences, Olympic Mountains, Washington. *Geological Society of America Bulletin*. 115: 1110-1121.

Bennett GL, Molnar P, McArdell BW, Burlando P. 2014. A probabilistic sediment cascade model of sediment transfer in the Illgraben. Water Resource Research 50: 1225-1244.

Berger C, McArdell BW, Schlunegger F. 2011. Sediment transfer patterns at the Illgraben catchment, Switzerland: implications for the time scales of debris flow activities. Geomorphology 125: 421-432.

Biodiversity Center of Japan. 2021. Natural Environmental Information GIS. Available at: http://gis.biodic.go.jp/webgis/.

Booth AM, Sifford C, Vascik B, Siebert C, Buma B. 2020. Large wood inhibits debris flow runout in forested southeast Alaska. Earth Surface Processes and Landforms 45: 1555–1568.

Bracken LJ, Turnbull L, Wainwright J, Bogaart P. 2015. Sediment connectivity: a framework for understanding sediment transfer at multiple scales. Earth Surface Processes and Landforms 40: 177-188.

Brideau MA, Stead D, Millard TH, Ward BC. 2019. Field characterisation and numerical modelling of debris avalanche runout on Vancouver Island, British Columbia, Canada. Landslides 16: 875-891.

Broeckx J, Rossi M, Lijnen K, Campforts B, Poesen J, Vanmaercke M. 2020. Landslide mobilization rates: A global analysis and model. Earth-Science Reviews 201: 102972.

Brzeziecki B, Kienast F. 1994. Classifying the life-history strategies of trees on the basis of the Grimian model. Forest Ecology and Management 69: 167-187.

Campforts B, Shobe CM, Steer P, Vanmaercke M, Lague D, Braun J. 2020. HyLands 1.0: a hybrid landscape evolution model to simulate the impact of

landslides and landslide-derived sediment on landscape evolution. Geoscientific Model Development 13: 3863–3886.

Capra L, Macias J, Scott K, Abrams M, Garduño-Monroy V. 2002. Debris avalanches and debris flows transformed from collapses in the Trans-Mexican Volcanic Belt, Mexico – behavior, and implications for hazard assessment. Journal of Volcanology and Geothermal Research 113: 81–110.

Chen Q, Baldocchi D, Gong P, Kelly M. 2006. Isolating individual trees in a savanna woodland using small footprint lidar data. Photogrammetric Engineering & Remote Sensing 72: 923–932.

Clauset A, Shalizi CR, Newman ME. 2009. Power-law distribution in empirical data. SIAM review 51: 661–703.

Crandell DR, Miller CD, Glicken HX, Christiansen RL, Newhall CG. 1984. Catastrophic debris avalanche from ancestral Mount Shasta volcano. Geology 12: 143–146.

Crandell DR. 1989. Gigantic debris avalanche of Pleistocene age from ancestral Mount Shasta volcano, California, and debris-avalanche hazard zonation. U.S. Geol. Surv. Bull. 1861: 32.

Dade WB, Huppert HE. 1998. Long-runout rockfall. Geology 26: 803–806.

D'Agostino V, Cesca M, Marchi L. 2010. Field and laboratory investigations of runout distances of debris flows in the Dolomites (Eastern Italian Alps). Geomorphology 115: 294–304.

Davies TR, McSaveney MJ. 1999. Runout of dry granular avalanches. Canadian Geotechnical Journal 36: 313–320.

De Haas T, Braat L, Leuven JR, Lokhorst IR, Kleinhans MG. 2015. Effects of debris flow composition on runout, depositional mechanisms, and deposit morphology in laboratory experiments. Journal of Geophysical Research: Earth Surface 120: 1949–1972.

Dowling CA, Santi PM. 2014. Debris flows and their toll on human life: a global analysis of debris-flow fatalities from 1950 to 2011. *Natural Hazards* 71: 203-227.

Dufresne A, Wolken GJ, Hibert C, Bessette-Kirton EK, Coe JA, Geertsema M, Ekström G. 2019. The 2016 Lamplugh rock avalanche, Alaska: deposit structures and emplacement dynamics. *Landslides* 16: 2301-2319.

Evans JR, Imaizumi F, Ohsaka O, Ogawa S. 2020. Relationship between tree height and landslide characteristics obtained by GIS assessment. Earth Surface Processes and Landforms 45: 3280-3292.

Fan X, Scaringi G, Korup O, West AJ, van Westen CJ, Tanyaş H, Hovius N, Hales TC, Jibson RW, Allstadt KE, Zhang L, Evans SG, Xu C, Li G, Pei X, Xu Q, Huang R. 2019a. Earthquake-induced chains of geologic hazards: patterns, mechanisms, and impacts. *Reviews of Geophysics* 57: 421-503.

Fan X, Xu Q, Scaringi G, Zheng G, Huang R, Dai L, Ju Y. 2019b. The "long" runout rock avalanche in Pusa, China, on August 28, 2017: a preliminary report. *Landslides* 16: 139-154.

Forestry Agency. 2019. Airborne laser scanning at forested areas in 2018 (part 1). Available at: https://www.maff.go.jp/j/budget/yosan_kansi/sikkou/tokutei_keihi/seika_H30/ippan/#189.

Francis PW, Gardeweg M, Ramirez CF, Rothery DA. 1985. Catastrophic debris avalanche deposit of Socompa volcano, northern Chile. *Geology* 13: 600-603.

Friele P, Millard TH, Mitchell A, Allstadt KE, Menounos B, Geertsema M, Clague JJ. 2020. Observations on the May 2019 Joffre Peak landslides, British Columbia. *Landslides* 17: 913-930.

Glade T. 2003. Landslide occurrence as a response to land use change: A review of evidence from New Zealand. Catena 51: 297-314.

Guzzetti F, Ardizzone F, Cardinali M, Rossi M, Valigi D. 2009. Landslide volumes and landslide mobilization rates in Umbria, central Italy. Earth and Planetary Science Letters 279: 222-229.

Guzzetti F, Mondini AC, Cardinali M, Fiorucci F, Santangelo M, Chang KT. 2012. Landslide inventory maps: new tools for an old problem. Earth-Science Reviews 112: 42-66.

Hampton MA, Lee HJ, Locat J. 1996. Submarine landslides. Reviews of Geophysics 34: 33–59.

Hayashi JN, Self S. 1992. A comparison of pyroclastic flow and debris avalanche mobility. Journal of Geophysical Research: Solid Earth 97: 9063–9071.

Hazlett RW, Buesch D, Anderson JL, Elan R, Scandone R. 1991. Geology, failure conditions, and implications of seismogenic avalanches of the 1944 eruption at Vesuvius, Italy. Journal of Volcanology and Geothermal Research 47: 249–264.

Hergarten S, Robl J, Stüwe K. 2014. Extracting topographic swath profiles across curved geomorphic features. Earth Surface Dynamics 2: 97–104.

Hergarten S, Robl J. 2021. A simple and efficient model for orographic precipitation. Geoscientific Model Development Discussion, in review, https://doi.org/10.5194/gmd-2021-179.

Hürlimann M, McArdell BW, Rickli C. 2015. Field and laboratory analysis of the runout characteristics of hillslope debris flows in Switzerland. Geomorphology 232: 20–32.

Iverson RM, Logan M, LaHusen RG, Berti M. 2010. The perfect debris flow? Aggregated results from 28 large-scale experiments. Journal of Geophysical Research: Earth Surface 115: F03005.

Iverson RM, George DL, Allstadt K, Reid ME, Collins BD, Vallance JW, Schilling SP, Godt JW, Cannon CM, Magirl CS, Baum RL, Coe JA, Schulz WH, Bower JB. 2015. Landslide mobility and hazards: implications of the 2014 Oso disaster. Earth and Planetary Science Letters 412: 197–208.

Iverson RM, George DL, Logan M. 2016. Debris flow runup on vertical barriers and adverse slopes. Journal of Geophysical Research: Earth Surface 121: 2333–2357.

Jackson CR, Sturm CA. 2002. Woody debris and channel morphology in first and second order forested channels in Washington's coast ranges. Water Resource Research 38: 1177–1190.

Johnson AC, Swanston DN, McGee KE. 2000. Landslide initiation, runout, and deposition within clearcuts and old-growth forests of Alaska. Journal of the American Water Resources Association 36: 17–30.

Johnson B. 1978. Blackhawk landslide, California, U.S.A. B. Voight (Ed.), Rockslides and Avalanches, Developments in geotechnical engineering, Elsevier Scientific Pub. Co, Amsterdam and New York: 481–504.

Kaibori M, Hasegawa Y, Yamashita Y, Sakida H, Nakai S, Kuwada S, Hiramatsu S, Jitousono T, Irasawa M, Shimizu O, Imaizumi F, Nakatani K, Kashiwabara Y, Kato N, Torita E, Hirakawa Y, Yoshinaga S, Tanaka K, Hayashi S. 2018. Sediment related disaster due to heavy rainfall in Hiroshima prefecture in July 2018. Journal of the Japan Society of Erosion Control Engineering 71 (5): 43-53 (in Japanese, with English abstract).

Korup O. 2005. Geomorphic imprint of landslides on alpine river systems, southwest New Zealand. *Earth Surface Processes and Landforms* 30 (7): 783-800.

Lancaster ST, Hayes SK, Grant GE. 2003. Effects of wood on debris flow runout in small mountain watersheds. Water Resources Research 39: 1168.

Larsen IJ, Montgomery DR, Korup O. 2010. Landslide erosion controlled by hillslope material. Nature Geoscience 3: 247-251.

Legros F. 2002. The mobility of long runout landslide. Engineering Geology 63: 301–331.

Li T. 1983. A mathematical model for predicting the extent of a major rockfall. Z. Geomorphol. 27: 473–482.

Li X, Yan Q, Zhao S, Luo Y, Wu Y, Wang D. 2020. Investigation of influence of baffles on landslide debris mobility by 3D material point method. Landslides 17: 1129–1143.

Lipman PW, Normark WR, Moore JG, Wilson JB, Gutmacher CE. 1988. The giant submarine Alika debris slide, Mauna Loa, Hawaii. Journal of Geophysical Research: Solid Earth 93: 4279–4299.

Liu X. 1996. Size of a debris flow deposition: model experiment approach. Environ. Geol. 28: 70–77.

Lucas A, Mangeney A, Ampuero JP. 2014. Frictional velocity-weakening in landslides on Earth and on other planetary bodies. Nature Communications 5: 3417.

Luccitta BK. 1978. A large landslide on Mars. Geol. Soc. Am. Bull., 89: 1601-1609.

Major JJ. 1997. Depositional processes in large-scale debris-flow experiments. J. Geol. 105: 345–366.

Major JJ, Iverson RM. 1999. Debris-flow deposition: Effects of pore-fluid pressure and friction concentrated at flow margins. Geological Society of America Bulletin 111: 1424–1434.

Malamud BD, Turcotte DL, Guzzetti F, Reichenbach P. 2004. Landslide inventories and their statistical properties. Earth Surface Processes and Landforms 29: 687–711.

Mark O, Behling R, Andermann C, Turowski JM, Illien L, Roessner S, Hovius N. 2019. Long-term erosion of the Nepal Himalayas by bedrock landsliding: the role of monsoons, earthquakes and giant landslides. Earth Surface Dynamics 7: 107–128.

May CL. 2002. Debris flows through different forest age classes in the central Oregon Coast Range. Journal of the American Water Resources Association 38: 1097–1113.

May CL, Gresswell RE. 2003a. Large wood recruitment and redistribution in headwater streams in the Southern Oregon Coast Range, USA. Canadian Journal of Forest Research 33: 1352–1362.

May CL, Gresswell RE. 2003b. Processes and rates of sediment and wood accumulation in headwater streams of the Oregon Coast Range, USA. Earth Surface Processes and Landforms 28: 409–424.

McEwen AS. 1989. Mobility of large rock avalanches: evidence from Valles Marineris, Mars. Geology. 17: 1111–1114.

McSaveney MJ. 1978. Sherman Glacier rock avalanche, Alaska, USA. B. Voight (Ed.), Rockslides and Avalanches, Developments in geotechnical engineering, Elsevier Scientific Pub. Co, Amsterdam and New York: 197–258.

Miller D, Luce C, Benda L. 2003. Time, space, and episodicity of physical disturbance in streams. Forest Ecology and Management 178: 121–140.

Naranjo JA, Francis P. 1987. High velocity debris avalanche at Lastarria volcano in the north Chilean Andes. Bull. Volcanol. 49: 509–514.

Petley D. 2012. Global patterns of loss of life from landslides. *Geology* 40: 927-930.

Piton G, Recking A. 2016. Design of sediment traps with open check dams. II: woody debris. Journal of Hydraulic Engineering 142: 1–17.

Potapov P, Li X, Hernandez-Serna A, Tyukavina A, Hansen MC, Kommareddy A, Pickens A, Turubanova S, Tang H, Silva CE, Armston J, Dubayah R, Blair JB,

Hofton M. 2021. Mapping global forest canopy height through integration of GEDI and Landsat data. Remote Sensing of Environment 253: 112165.

Pudasaini SP, Miller SA. 2013. The hypermobility of huge landslides and avalanches. Engineering Geology 157: 124–137.

R Core Team. 2022. R: A Language and Environment for Statistical Computing. https://www.r-project.org/.

Ruiz-Villanueva V, Díez-Herrero A, Ballesteros JA, Badoque JM. 2014. Potential large woody debris recruitment due to landslides, bank erosion and floods in mountain basins: a quantitative estimation approach. River Research and Applications 30: 81–97.

Ruiz-Villanueva V, Piégay H, Gurnell AM, Marston RA, Stoffel M. 2016. Recent advances quantifying the large wood dynamics in river basins: New methods and remaining challenges. Reviews of Geophysics 54: 611–652.

Sankey T, Shrestha R, Sankey JB, Hardegree S, Strand E. 2013. Lidar-derived estimate and uncertainty of carbon sink in successional phases of woody encroachment. Journal of Geophysical Research: Biogeosciences 118: 1144–1155.

Siebe C, Komorowski JC, Sheridan MF. 1992. Morphology and emplacement of an unusual debris-avalanche deposit at Jocotitlán volcano, Central Mexico. Bull. Volcanol. 54: 573–589.

Siebert L. 1984. Large volcanic debris avalanches: Characteristics of source areas, deposits, and associated eruptions. Journal of Volcanology and Geothermal Research 22: 163–197.

Siebert L, Glicken H, Ui T. 1987. Volcanic hazards from Bezymianny- and Bandai-type eruptions. Bull. Volcanol. 49: 435–459.

Staley DM, Wasklewicz TA, Kean JW. 2014. Characterizing the primary material sources and dominant erosional processes for post-fire debris-flow initiation in a headwater basin using multi-temporal terrestrial laser scanning data. Geomorphology 214: 324-338.

Stoopes GR, Sheridan MF. 1992. Giant debris avalanches from the Colima Volcanic complex, Mexico: implications for long-runout landslides (>100 km) and hazard assessment. Geology 20: 299-302.

Swayze NC, Tinkham WT, Vogeler JC, Hudak AT. 2021. Influence of flight parameters on UAS-based monitoring of tree height, diameter, and density. Remote Sensing of Environment 263: 112540.

Swanson FJ, Gregory SV, Iroumé A, Ruiz-Villanueva V, Wohl E. 2021. Reflection on the history of research on large wood in rivers. Earth Surface Processes and Landforms 46: 55–56.

Tang YJ, Xu ZM, Yang TQ, Zhou ZH, Wang K, Ren Z, Yang K, Tian L. 2018. Impacts of small woody debris on slurrying, persistence, and propagation in a low-gradient channel of the Dongyuege debris flow in Nu River, Southwest China. Landslides 15: 2279–2293.

Tanyaş H, van Westen CJ, Allstadt KE, Jibson RW. 2019. Factors controlling landslide frequency–area distributions. *Earth Surface Processes and Landforms* 44(4): 900-917.

Tsunetaka H. 2021. Comparison of the return period for landslide□triggering rainfall events in Japan based on standardization of the rainfall period. Earth Surface Processes and Landforms 46: 2984–2998.

Tsunetaka H, Mtibaa S, Asano S, Okamoto T, Kurokawa U. 2021. Comparison of length and dynamics of wood pieces in streams covered with coniferous and broadleaf forests mapped using orthophotos acquired by an unmanned aerial vehicle. Progress in Earth and Planetary Science 8: 22.

Vilén T, Gunia K, Verkerk PJ, Seidl R, Schelhaas MJ, Lindner M, Bellassen V. 2012. Reconstructed forest age structure in Europe 1950–2010. Forest Ecology and Management 286: 203-218.

Voight B, Janda RJ, Glicken H, Douglass PM. 1983. Nature and mechanics of the Mount St Helens rockslide-avalanche of 18 May 1980. Géotechnique 33: 243-273.

Walter F, Amann F, Kos A, Kenner R, Phillips M, de Preux A, Huss M, Tognacca C, Clinton J, Diehl T, Bonanomi Y. 2020. Direct observations of a three million cubic meter rock-slope collapse with almost immediate initiation of ensuing debris flows. Geomorphology 351: 106933.

Weller DE. 1987. Self-thinning exponent correlated with allometric measures of plant geometry. Ecology 68: 813–821.

Westoby M. 1984. The self-thinning rule. Advances in ecological research 14: 167–225.

Wohl E, Ogden FL, Goode J. 2009. Episodic wood loading in a mountainous neotropical watershed. Geomorphology 111: 149–159.

Yoda K. 1963. Self-thinning in overcrowded pure stands under cultivated and natural conditions (Intraspecific competition among higher plants. XI). J. Inst. Polytech. Osaka City Univ. Ser. D. 14: 107–129.

Yun T, Jiang K, Li G, Eichhorn MP, Fan J, Liu F, Chen B, An F, Cao L. 2021. Individual tree crown segmentation from airborne LiDAR data using a novel Gaussian filter and energy function minimization-based approach. Remote Sensing of Environment 256: 112307.

Zhen Z, Quackenbush LJ, Stehman SV, Zhang L. 2015. Agent-based region growing for individual tree crown delineation from airborne laser scanning (ALS) data. International Journal of Remote Sensing 36: 1965–1993.

Figure captions

Figure 1. Study site: (a) overview and (b) location of the study area. The areas indicated in red correspond to areas where both DEMs and DSMs were available before the landslide event (measured in February 2015) and after the landslide event (measured in October 2018).

Figure 2. Graphical illustration of the definitions of the runout distance and the drop height. Panel (a) shows frequently used parameters: *H* indicates the total drop height (i.e., the elevation distance from the top of the landslide scar to the lower end of the deposition area) and *L* indicates the total runout distance (i.e., the projected horizontal distance from the top of the landslide scar to the lower end of the deposition area). Panel (b) shows the parameters that were used in this study. *H′* and *L′* indicate the drop height and the runout distance, respectively, from the top of the landslide scar to the upper end of the deposition area.

Figure 3. Histogram of the runout distance (*L*') of the landslide inventory. The blue line and the dashed red line indicate the cumulative distribution and the mean value, respectively.

Figure 4. Graphical illustration of the definitions of the tree-height (*TH*) indices. Panel (a) indicates a sample of observation points (the yellow points) for a swath profile corresponding to a mapped runout area (the red line). The observation points were for a width of 30 m and at a resolution of 1 m. The crown-height model (CHM) in the background indicates the tree height after the landslide event (taller and shorter trees are expressed by light and dark colours, respectively). Panel (b) indicates the swath profile calculated by the CHM based on the setting shown in panel (a). The red and blue lines indicate the highest and lowest extremes, respectively. The black line indicates the mean values. The TH_{max} (the red dotted line), TH_{mean} (the dotted black line), and TH_{min} (the dotted blue line) values are the average of the highest extremes, the mean values, and the lowest extremes, respectively.

Figure 5. Scaling relationships between the landslide area (*A*) and the volume (*V*) on the log–log *V*–*A* plane. The thick black line indicates the power-law scaling relationship for the landslide area–volume data (*n* = 366). The thin black lines are plotted assuming landslide depths of 0.1, 1, or 10 m.

Figure 6. Boxplots of the landslide depth and slopes of the landslide scars. Panel (a) shows the mean landslide depth and panel (b) shows the mean slope of the landslide scars before and after the landslide event. The thick black line in the boxes indicates the median. Outliers are expressed as small points.

Figure 7. Frequency area distribution (FAD) for the landslide area. The cut-off and β values were estimated using the method proposed by Clauset et al. (2009).

Figure 8. Relationships between the average tree height at the landslide scar and (a) the landslide area and (b) the landslide volume.

Figure 9. Relationships between the runout distance (*L'*) and (a) the landslide area and (b) the landslide volume on the log–log plane. The black line indicates the power-law scaling relationship for the landslide runout distance to the area or volume data.

Figure 10. Relationships between the runout distance (*L'*) and the tree-height (*TH*) indices. The left and right panels indicate the *TH* indices obtained before and after the landslide event, respectively: (a, b) TH_{min}, (c, d) TH_{mean}, and (e, f) TH_{max}. The vertical red line indicates the average runout distance (115.0 m).

Figure 11. Boxplots of the landslide and tree-height properties for long-runout (L' > 115.0 m) and short-runout (L' ≤ 115.0) landslides: (a, b) TH_{min}, (c, d) TH_{mean}, and (e, f) TH_{max}. Panels (a–c) indicate the area, volume, and average tree height of the landslide scars, respectively. In panels (d–i), the left panels indicate the *TH* indices before the 2018 landslide event whereas the right panels indicate *TH* indices after the 2018 landslide event. The thick black line in the boxes indicates the median. Outliers are expressed as small points. Note that, in panel (b), the largest outlier (12,665.0 m^3) is not plotted. The *p*-values indicate the result of the Wilcoxon–Mann–Whitney test between the long- and short-runout landslides.

Figure 12. Principal component analysis (PCA) result showing the principal component scores and loadings for the first two principal components (PC1 and PC2). Labels abbreviations are Area: Landslide area; Volume: landslide volume; Tree: average tree height of the landslide scar; $TH_{min\ before}$: TH_{min} before the landslide event; $TH_{min\ after}$: TH_{min} after the landslide event; $TH_{mean\ before}$: TH_{mean} before the landslide event; $TH_{mean\ after}$: TH_{mean} after the landslide event; $TH_{max\ before}$: TH_{max} before the landslide event; and $TH_{max\ after}$: TH_{max} after the landslide event. The red and blue plots indicate the long-runout (L' > 115.0 m) and short-runout (L' ≤ 115.0) landslides, respectively.

Figure 13. Relationship between TH_{min} and TH_{max}. Panels (a) and (b) indicate the *TH* indices obtained before and after the landslide event, respectively. The red and blue plots indicate the long-runout (L' > 115.0 m) and short-runout (L' ≤ 115.0) landslides, respectively.

Figure 14. Relationships between the runout distance and the drop height. The thin black lines assume a mobility of 1, 2, 5, 10, 20, or 35, which reflects the typical mobility of surface terrestrial landslides. Data concerning surface terrestrial landslides (n = 525) are from Abele, 1974; Johnson, 1978; Luccitta, 1978; McSaveney, 1978; Li, 1983; Voight et al., 1983; Crandell et al., 1984; Siebert, 1984; Francis et al., 1985; Naranjo and Francis, 1987; Siebert et al., 1987; Crandell, 1989; Hazlett et al., 1991; Hayashi and Self, 1992; Siebe et al., 1992; Stoopes and Sheridan, 1992; Davies and McSaveney, 1999; Capra et al.,

2002; D'Agostino et al., 2010; Iverson et al., 2015; Brideau et al., 2019; Dufresne et al., 2019; Fan et al., 2019b; Friele et al., 2020; and Walter et al., 2020. Data concerning experiments (*n* = 462) are from Liu, 1996; Major, 1997; D'Agostino et al., 2010; Iverson et al., 2010; De Haas et al., 2015; Hürlimann et al., 2015; and Baselt et al., 2022. Data concerning submarine landslides (*n* = 44) are from Lipman et al., 1988, and Hampton et al., 1996. Data concerning Martian landslides (*n* = 30) are from Luccitta, 1978, and McEwen, 1989.

Figure 15. Landslide volume versus mobility. Data concerning surface terrestrial landslides (*n* = 336) are from Abele, 1974; Johnson, 1978; Luccitta, 1978; McSaveney, 1978; Li, 1983; Voight et al., 1983; Crandell et al., 1984; Siebert, 1984; Francis et al., 1985; Naranjo and Francis, 1987; Siebert et al., 1987; Crandell, 1989; Hazlett et al., 1991; Hayashi and Self, 1992; Siebe et al., 1992; Stoopes and Sheridan, 1992; Davies and McSaveney, 1999; Capra et al., 2002; D'Agostino et al., 2010; Iverson et al., 2015; Brideau et al., 2019; Dufresne et al., 2019; Fan et al., 2019b; Friele et al., 2020; and Walter et al., 2020. Data concerning experiments (*n* = 462) are from Liu, 1996; Major, 1997; D'Agostino et al., 2010; Iverson et al., 2010; De Haas et al., 2015; Hürlimann et al., 2015; and Baselt et al., 2022. Data concerning submarine landslides (*n* = 30) are from Lipman et al., 1988 and Hampton et al., 1996. Data concerning Martian landslides (*n* = 27) are from Luccitta, 1978 and McEwen, 1989. Note that the sample numbers for these categories, apart from the experimental data, are smaller than those in Figure 14 because it is sometimes difficult to constrain the initial landslide volume (the volume of landslide scar) in natural settings.

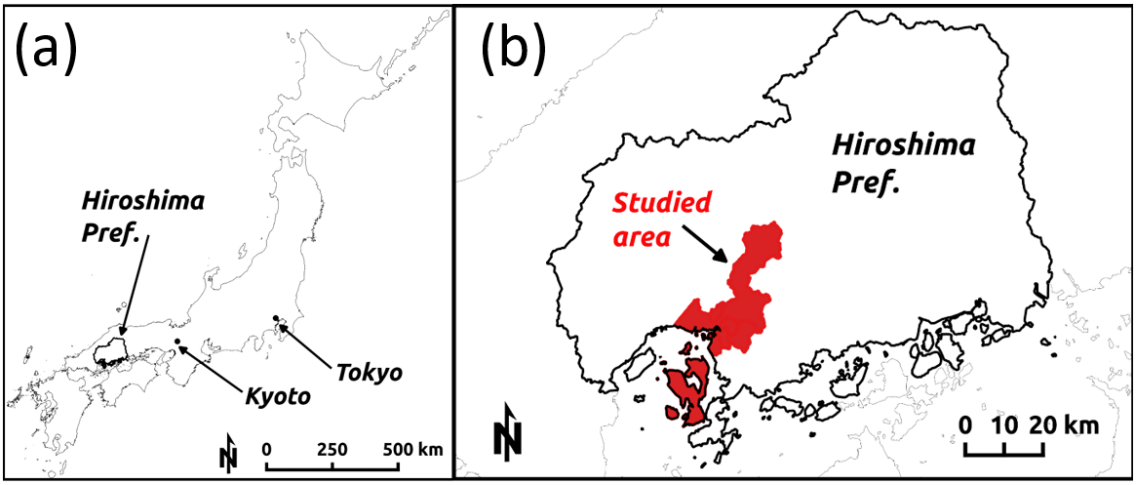

Figure 1. Study site. (a) overview and (b) location of the study area. The area indicated by red corresponds to the area where both DEMs and DSMs were available for before the landslide event (measured in February 2015) and after the landslide event (measured in October 2018).

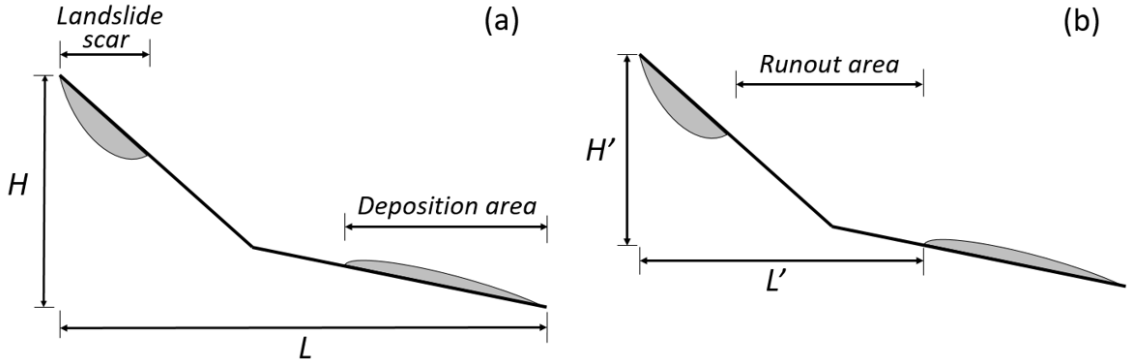

Figure 2 Graphical illustration of the definitions of the runout distance and the drop height. (a) shows the frequently used parameters: *H* indicates the total drop height (i.e., the elevation distance from the top of the landslide scar to the lower end of the deposition area); *L* indicates the total runout distance (i.e., the vertically projected distance from the top of the landslide scar to the lower end of the deposition area). (b) shows the parameters that were used in this study. *H′* and *L′* indicate the drop height and the runout distance from the top of the landslide scar to the upper end of the deposition area, respectively.

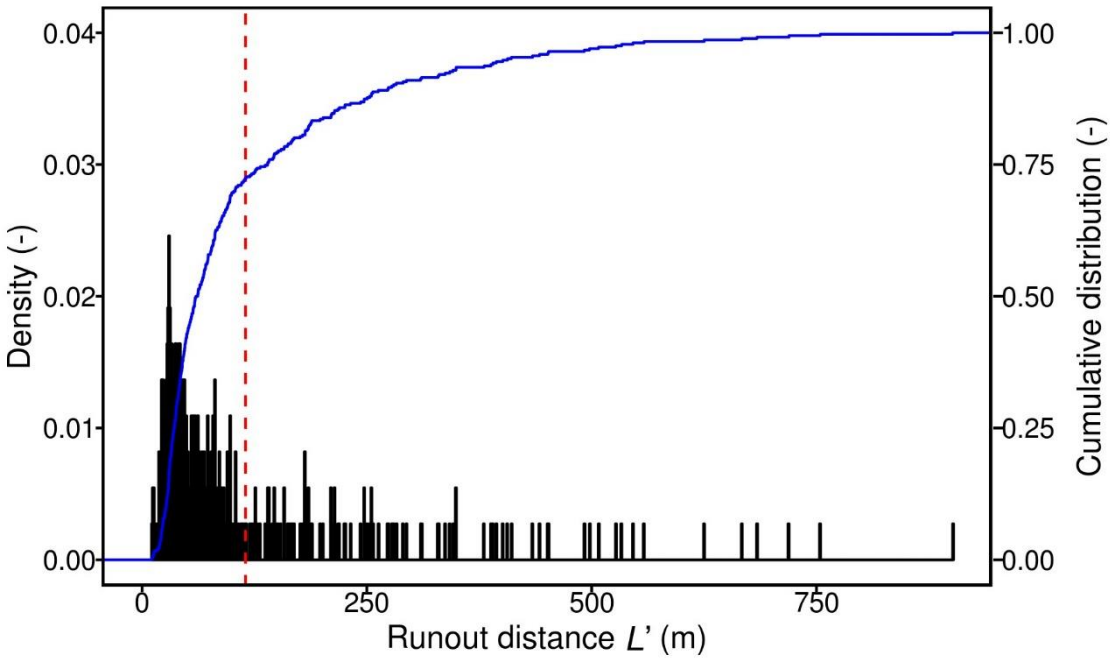

Figure 3 Histogram of runout distance (*L*') of the landslide inventory. The blue line and dashed red line indicate the cumulative distribution and the mean value, respectively.

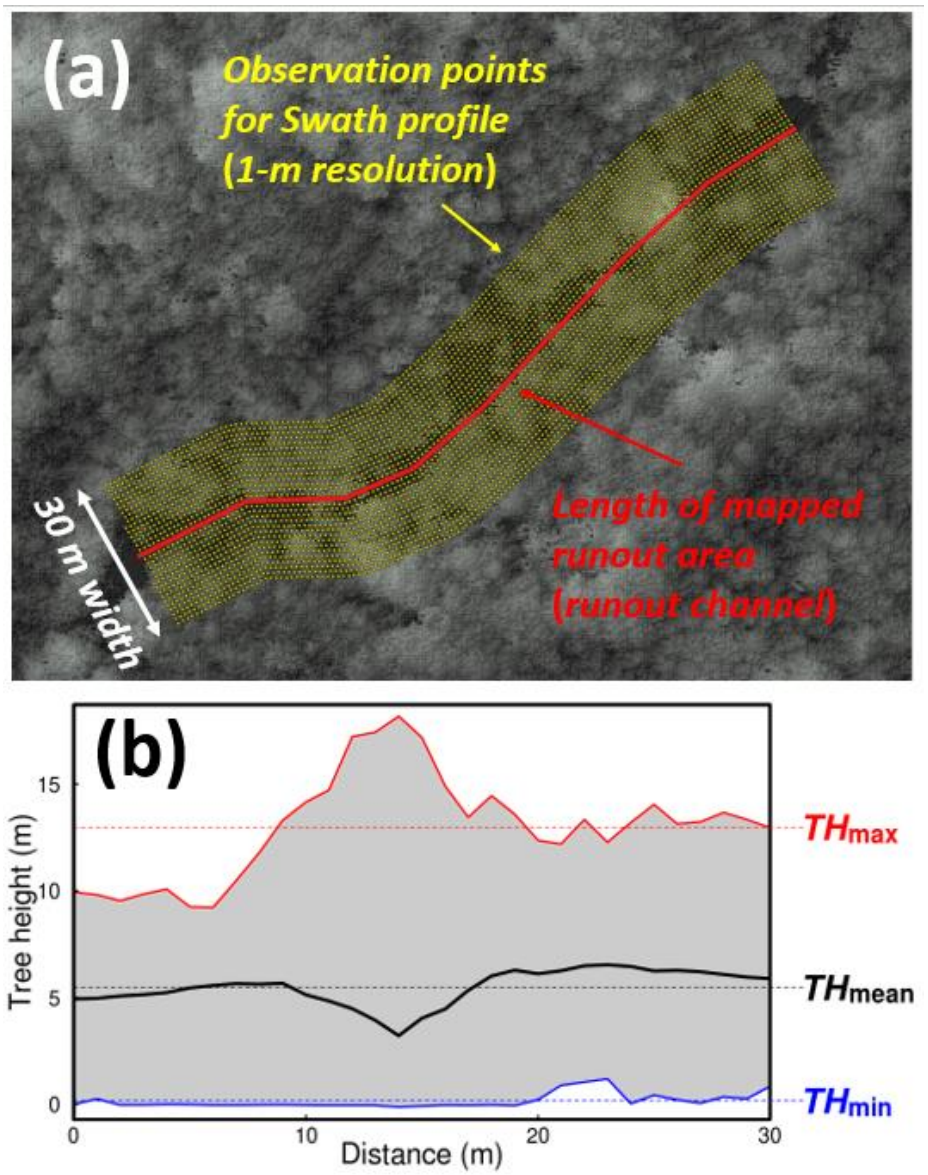

Figure 4 Graphical illustration of the definitions of the tree height (*TH*) indices. (a) indicates a sample of the observation points (the yellow points) for a swath profile corresponding to a mapped runout area (the red line). The observation points were at a width of 30 m and a resolution of 1 m. The CHM in the background indicates the tree height after the landslide event (taller and shorter trees are expressed by light and dark colours, respectively). (b) indicates the swath profile calculated by the CHM based on the setting shown in panel (a). The red and blue lines indicate the highest and lowest extremes, respectively. The black line indicates the mean values. The TH_{max} (the red dotted line), TH_{mean} (the dotted black line), and TH_{min} (the dotted blue line) are the average of the highest extremes, the mean values, and the lowest extremes, respectively.

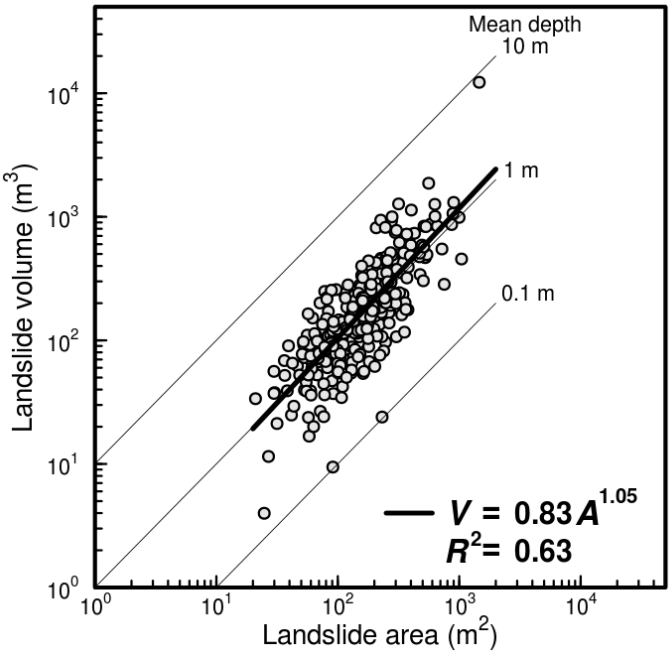

Figure 5 Scaling relationships between the landslide area (*A*) and the volume (*V*) on the log-log *V*-*A* plane. The thick black line indicates the power-law scaling relationship for the landslide area-volume data (*n* = 366). The thin black lines are graphs that assume landslide depths of 0.1, 1, or 10 m.

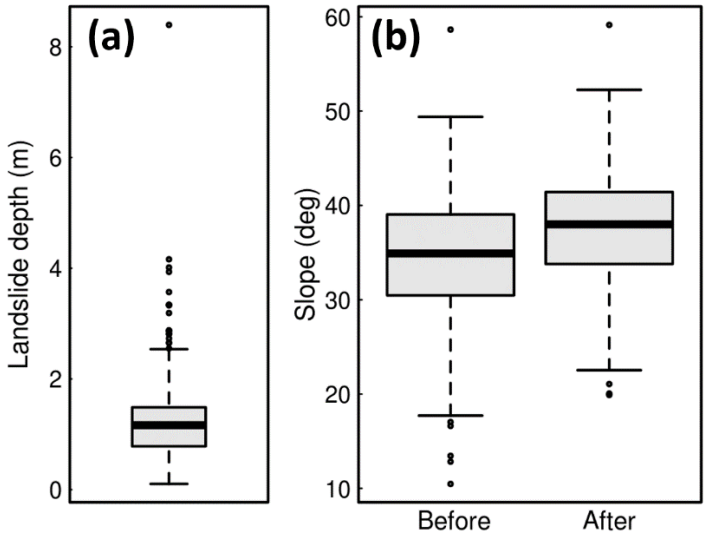

Figure 6 Boxplots of the landslide depth and slopes of the landslide scars. (a) shows the mean landslide depth and (b) shows the mean slope of landslide scars before and after the landslide event. The thick black line in the boxes indicates the median. Outliers are expressed as small points.

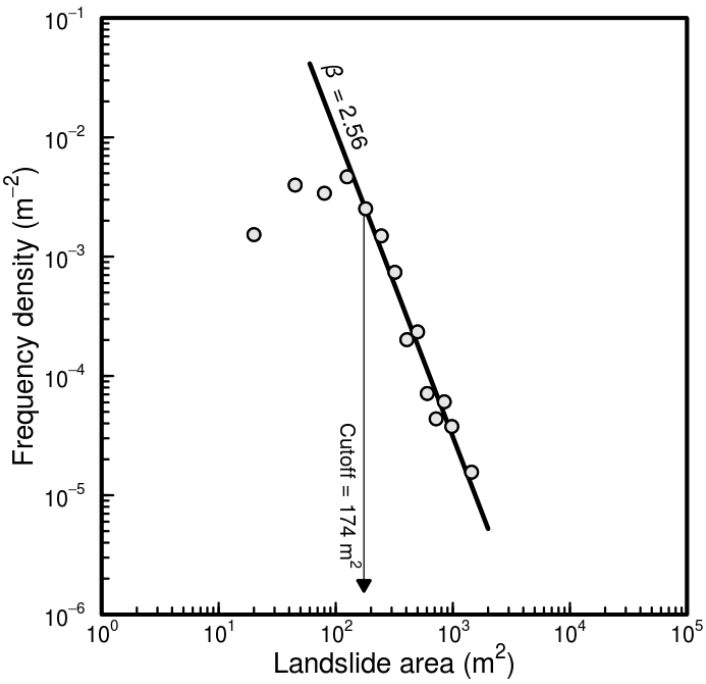

Figure 7 Frequency area distribution (FAD) for the landslide area. Cutoff and *β* values were estimated by the method proposed by Clauset et al. (2009).

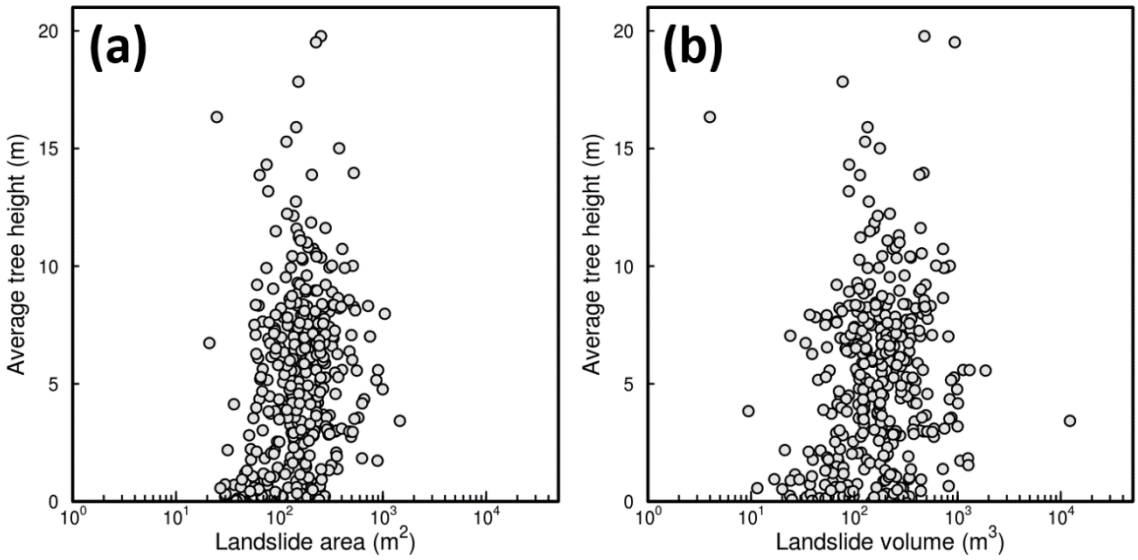

Figure 8 Relationship between the average tree height at the landslide scar and (a) the landslide area and (b) the landslide volume.

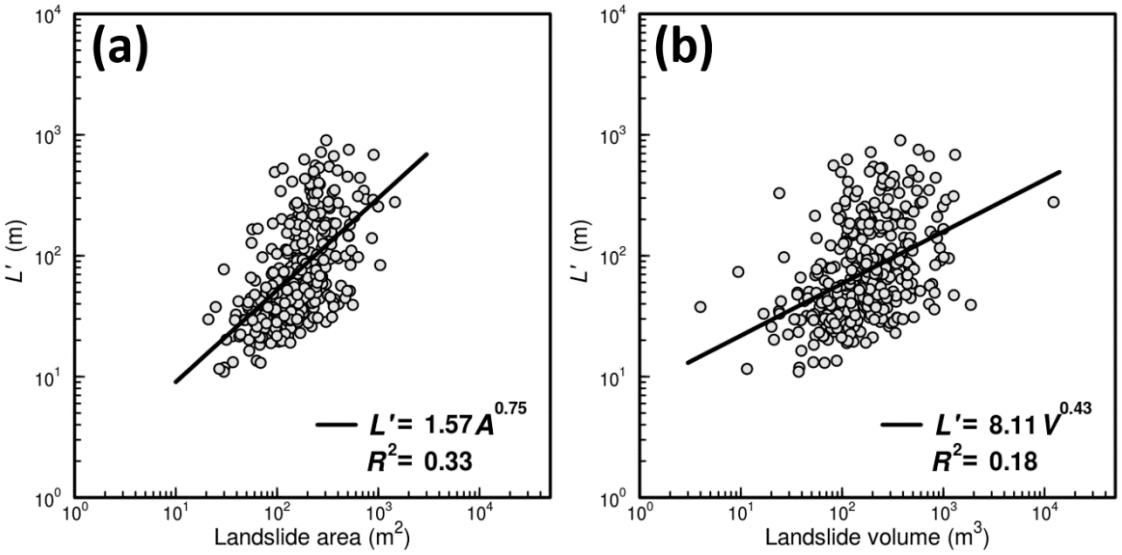

Figure 9 Relationship between the runout distance (*L′*) and (a) the landslide area and (b) the landslide volume on the log-log plane. The black line indicates the power-law scaling relationship for the landslide runout distance to area or volume data.

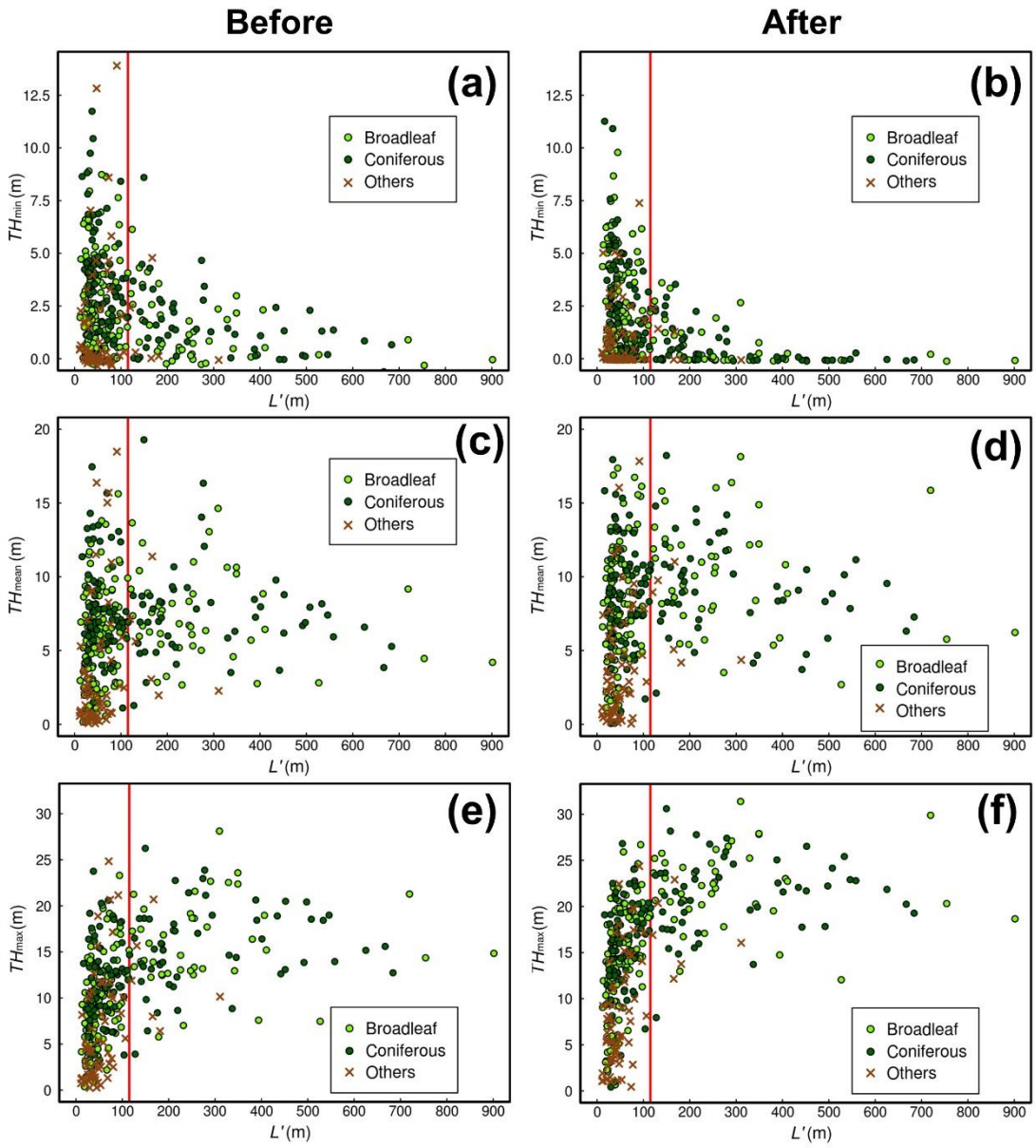

Figure 10 Relationship between the runout distance (*L'*) and the tree height (*TH*) indices. The left and right panels indicate the *TH* indices obtained before and after the landslide event, respectively. (a, b) TH_{min}, (c, d) TH_{mean}, and (e, f) TH_{max}. The vertical red line indicates the average runout distance (115.0 m).

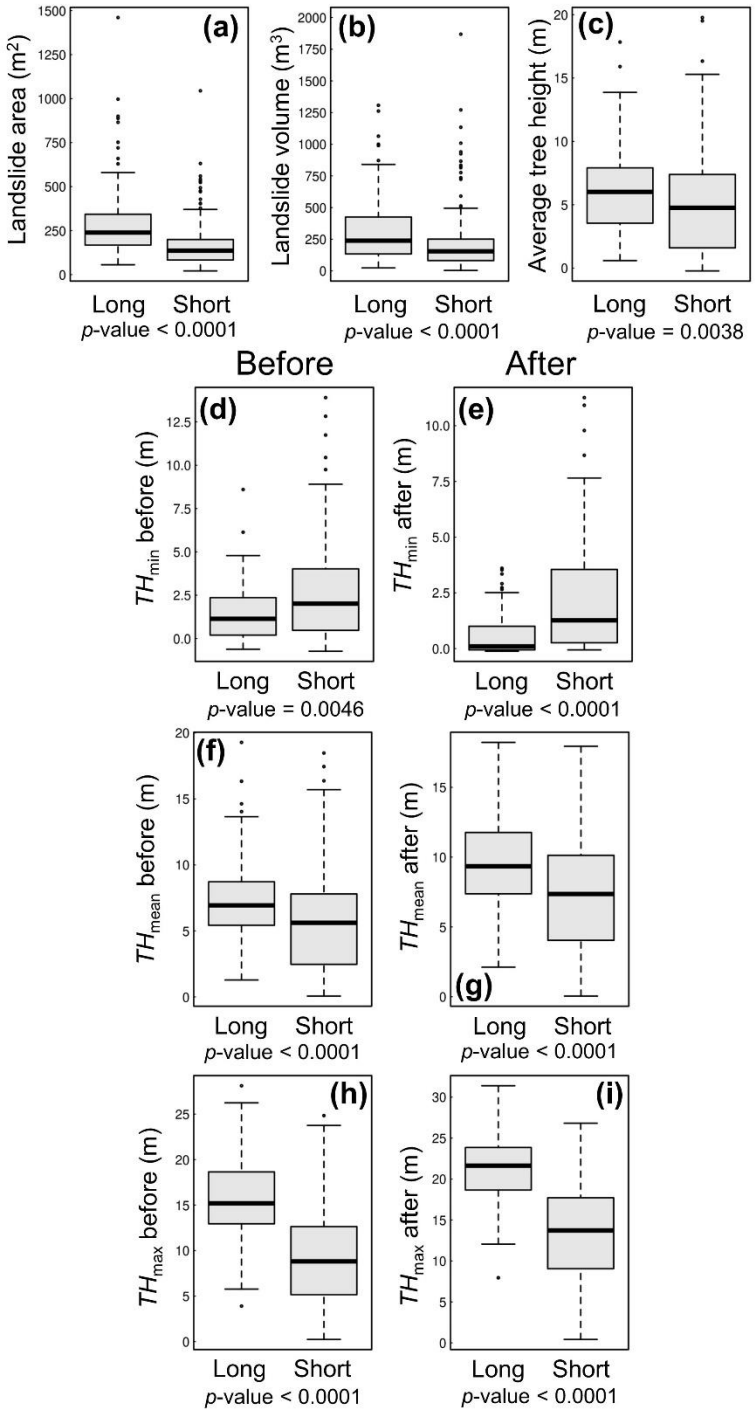

Figure 11 Boxplots of the landslide and tree-height properties for long- (L' >115.0 m) and short-runout (L' ≤115.0) landslides. (a–c) Area, volume, and average tree height of landslide scars, respectively. (d–i) the left panels indicate the *TH* indices before the landslide event in 2018 whereas the right panels indicate *TH* indices after the landslide event in 2018. (a, b) TH_{min}, (c, d) TH_{mean}, and (e, f) TH_{max}. The thick black line in the boxes indicates the median. Outliers are expressed as small points. Note that in panel b, the largest outlier (12665.0 m^3) is not expressed. The p-values indicate the result of the Wilcoxon-Mann-Whitney test between the long- and short-runout landslides.

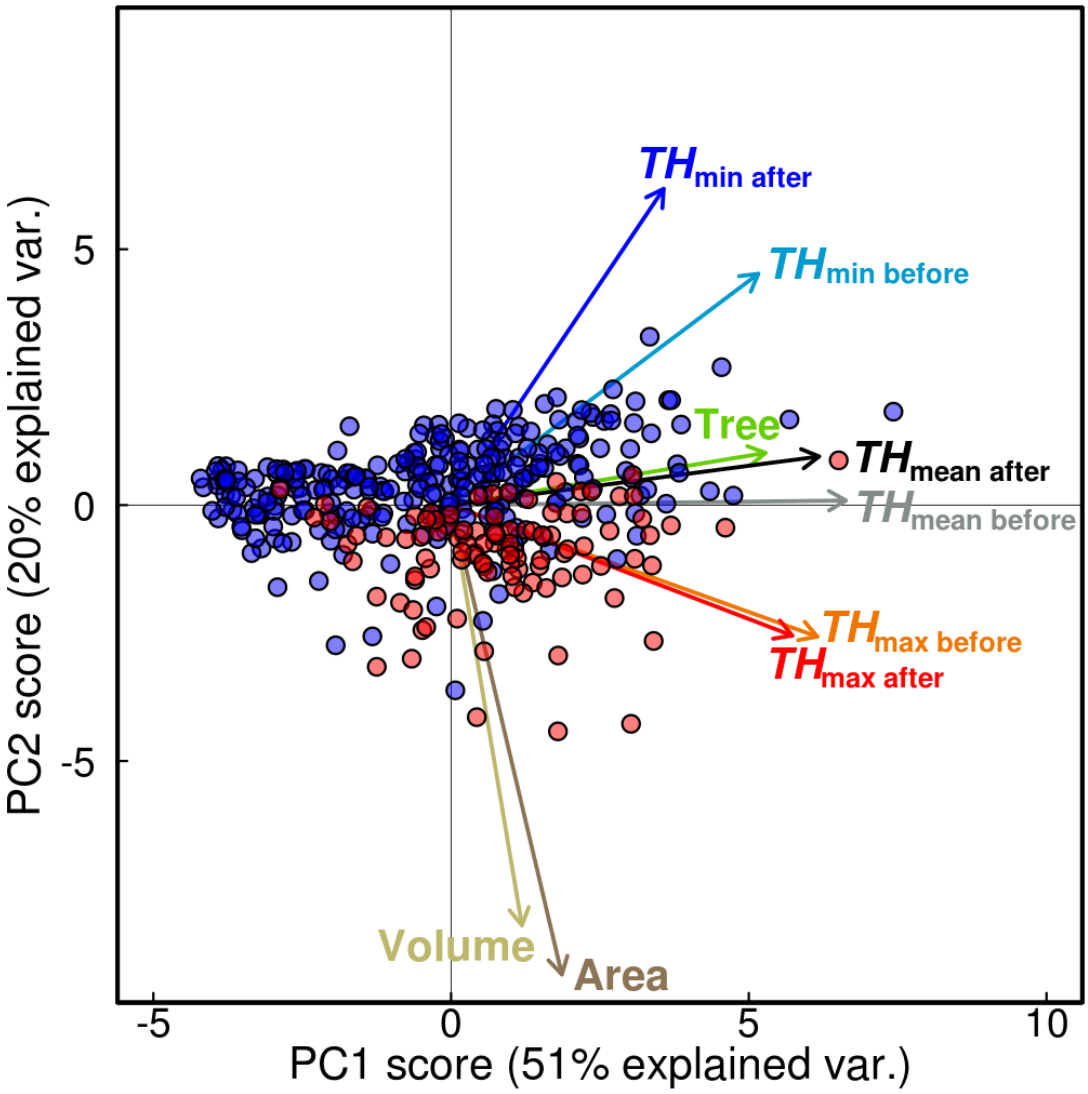

Figure 12 PCA result showing principal component scores and loadings for the first two principal components (PC1–PC2). Labels abbreviations: Area: Landslide area, Volume: landslide volume, Tree: average tree height of the landslide scar, $TH_{min\ before}$: TH_{min} before the landslide event, $TH_{min\ after}$: TH_{min} after the landslide event, $TH_{mean\ before}$: TH_{mean} before the landslide event, $TH_{mean\ after}$: TH_{mean} after the landslide event, $TH_{max\ before}$: TH_{max} before the landslide event, $TH_{max\ after}$: TH_{max} after the landslide event, Red and blue plots indicate the long- (L' >115.0 m) and short-runout (L' ≤115.0) landslides, respectively.

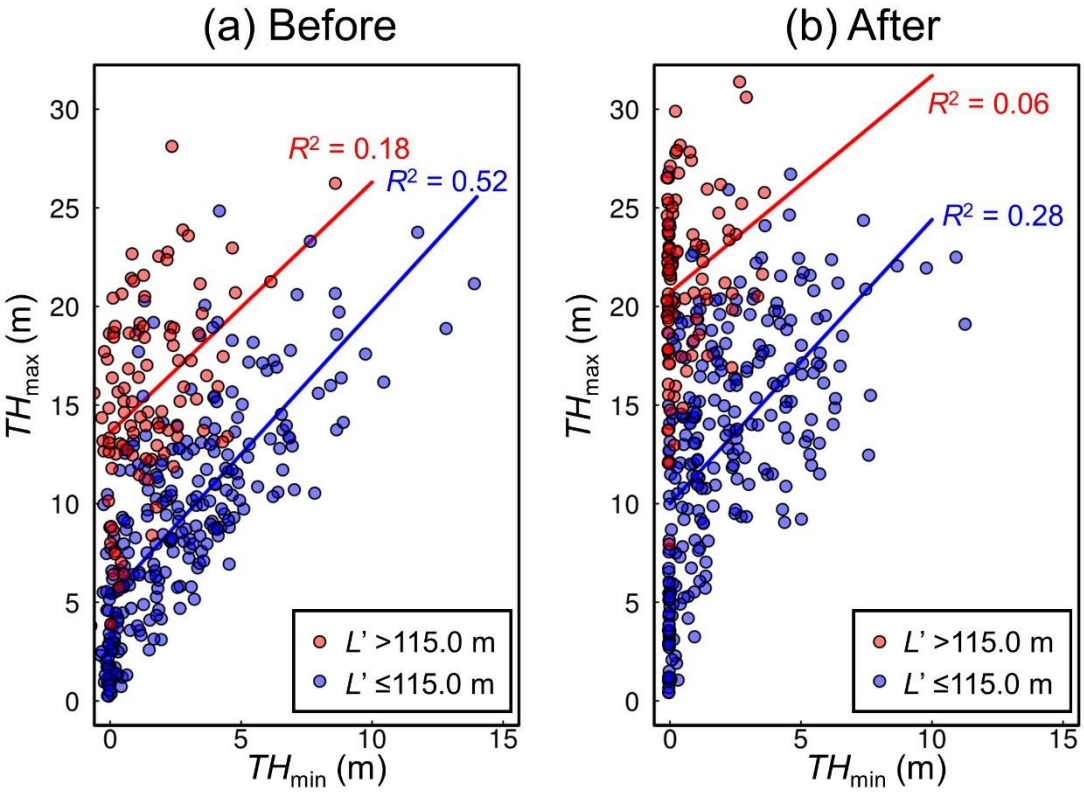

Figure 13 Relationship between TH_{min} and TH_{max}. Panels (a) and (b) indicate the *TH* indices obtained before and after the landslide event, respectively. Red and blue plots indicate the long- (L' >115.0 m) and short-runout (L' ≤115.0) landslides, respectively.

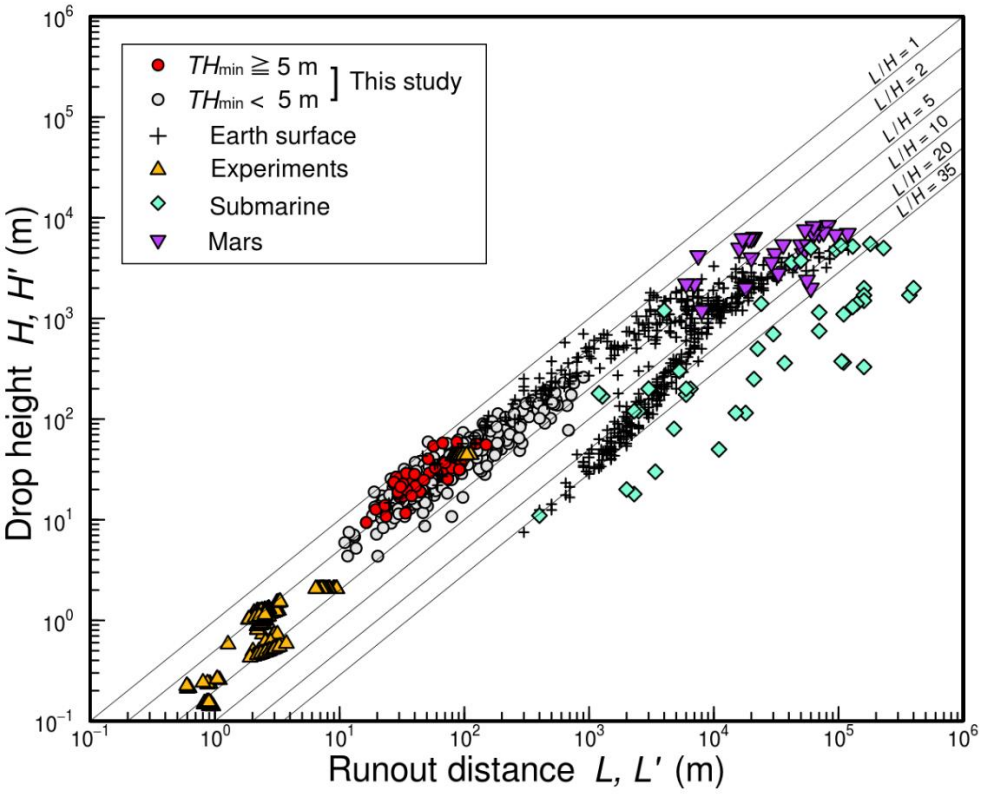

Figure 14 Relationships between the runout distance and drop height. The thin black lines are graphs that assume the mobility is 1, 2, 5, 10, 20, or 35, which reflects the typical mobility of landslides on the earth's surface. Data of landslides on the earth's surface (n = 525) are from Abele, 1974; Johnson, 1978; Luccitta, 1978; McSaveney, 1978; Li, 1983; Voight et al., 1983; Crandell et al., 1984; Siebert, 1984; Francis et al., 1985; Naranjo and Francis, 1987; Siebert et al., 1987; Crandell, 1989; Hazlett et al., 1991; Hayashi and Self, 1992; Siebe et al., 1992; Stoopes and Sheridan, 1992; Davies and McSaveney, 1999; Capra et al., 2002; D'Agostino et al., 2010; Iverson et al., 2015; Brideau et al., 2019; Dufresne et al., 2019; Fan et al., 2019b; Friele et al., 2020, and Walter et al., 2020. Data of experiments (n = 462) are from Liu, 1996; Major, 1997; D'Agostino et al., 2010; Iverson et al., 2010; De Haas et al., 2015; Hürlimann et al., 2015, and Baselt et al., 2022. Data of submarine landslides (n = 44) are from Lipman et al., 1988, and Hampton et al., 1996. Data of Martian landslides (n = 30) are from Luccitta, 1978, and McEwen, 1989.

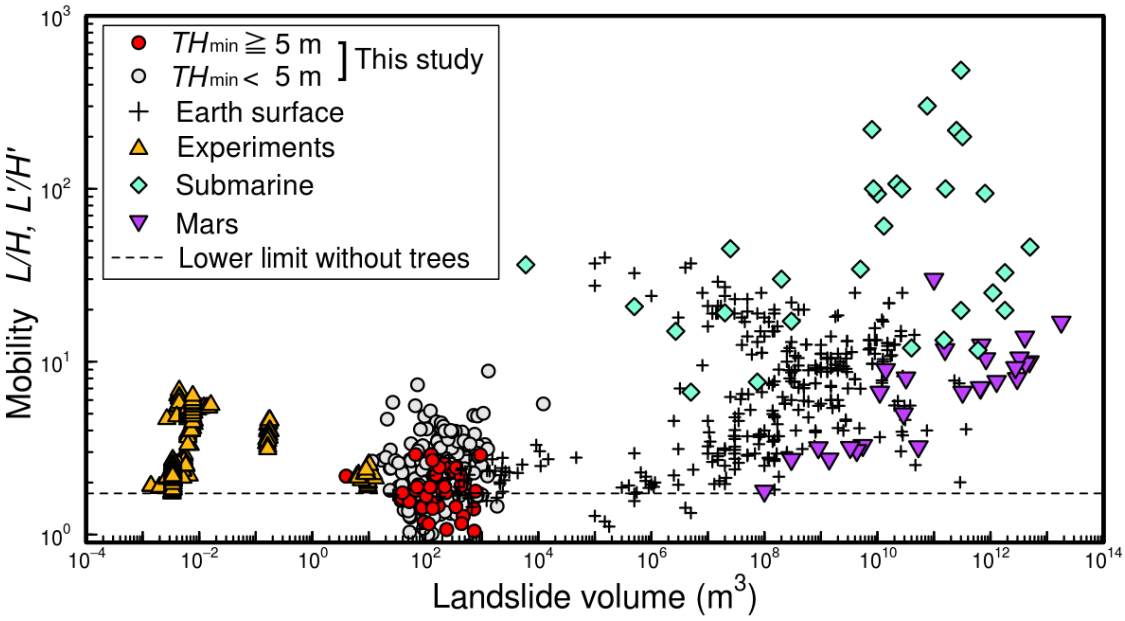

Figure 15 Landslide volume versus mobility. Data from landscapes on the earth's surface (*n* = 336) are from Abele, 1974; Johnson, 1978; Luccitta, 1978; McSaveney, 1978; Li, 1983; Voight et al., 1983; Crandell et al., 1984; Siebert, 1984; Francis et al., 1985; Naranjo and Francis, 1987; Siebert et al., 1987; Crandell, 1989; Hazlett et al., 1991; Hayashi and Self, 1992; Siebe et al., 1992; Stoopes and Sheridan, 1992; Davies and McSaveney, 1999; Capra et al., 2002; D'Agostino et al., 2010; Iverson et al., 2015; Brideau et al., 2019; Dufresne et al., 2019; Fan et al., 2019b; Friele et al., 2020, and Walter et al., 2020. Data of experiments (*n* = 462) are from Liu, 1996; Major, 1997; D'Agostino et al., 2010; Iverson et al., 2010; De Haas et al., 2015; Hürlimann et al., 2015, and Baselt et al., 2022. Data of submarine landslides (*n* = 30) are from Lipman et al., 1988 and Hampton et al., 1996. Data of Martian landslides (*n* = 27) are from Luccitta, 1978 and McEwen, 1989. Note that the sample numbers for these categories, apart from the experimental data, are lower than in Figure 10 because it is sometimes difficult to constrain the initial landslide volume (volume of landslide scar) in natural settings.

Supporting Information: Supplementary Material

Do standing trees affect landslide mobility on forested hillslopes in Japan?

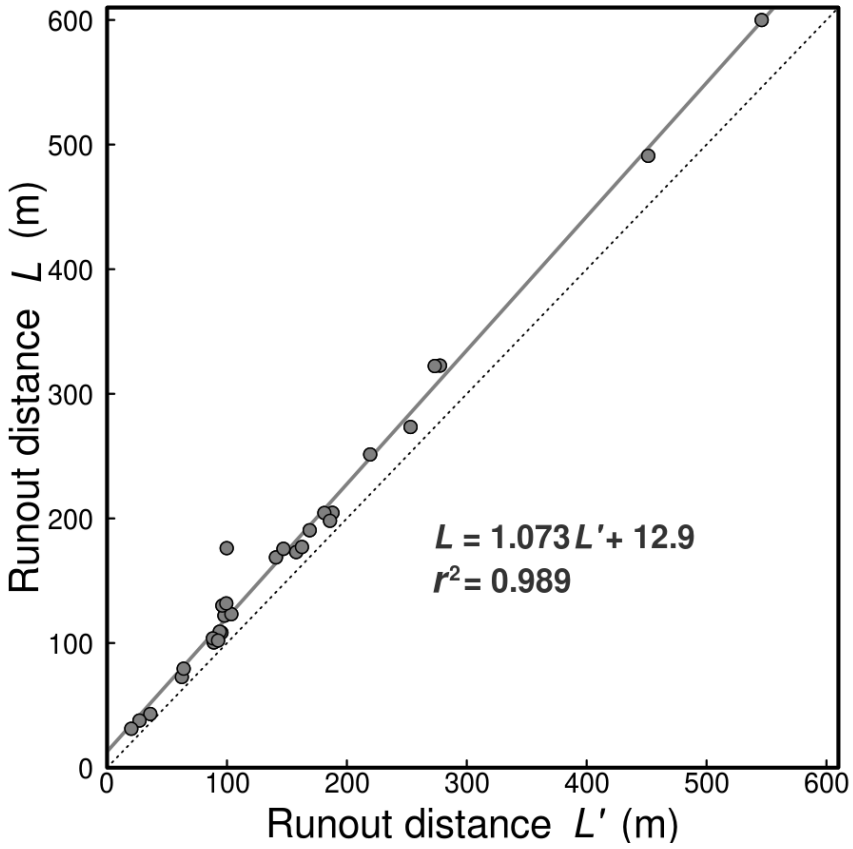

Figure S1. Comparison between *L′* and *L*. The solid line indicates the linear regression line. The dotted line indicates 1:1 agreement between *L′* and *L*.

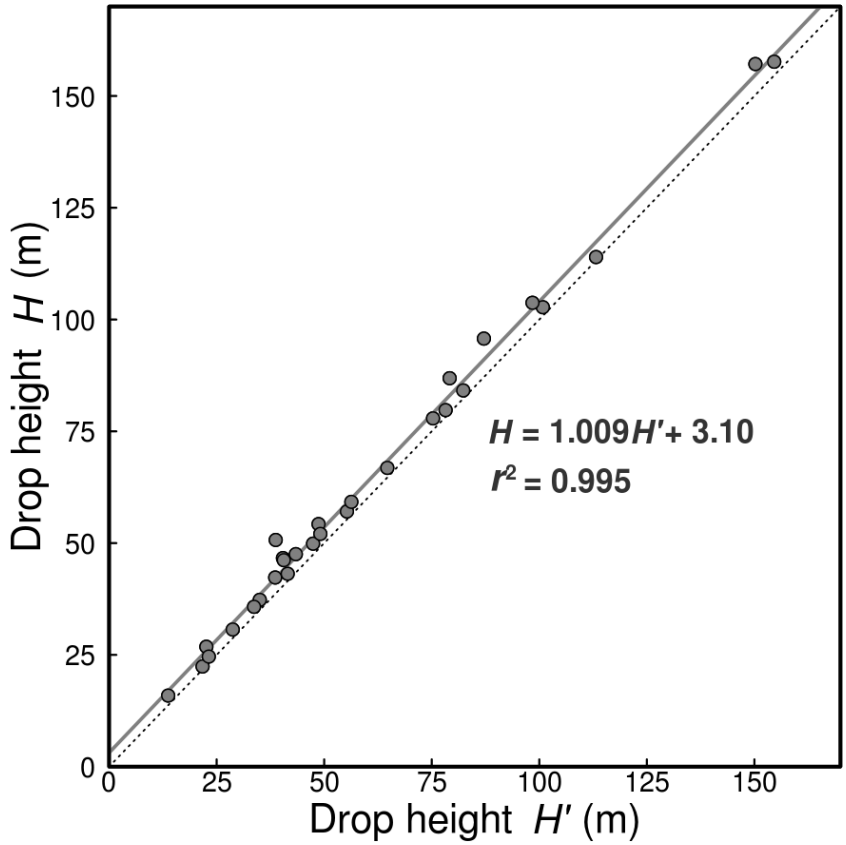

Figure S2. Comparison between *H′* and *H*. The solid line indicates the linear regression line. The dotted line indicates 1:1 agreement between *H′* and *H*.

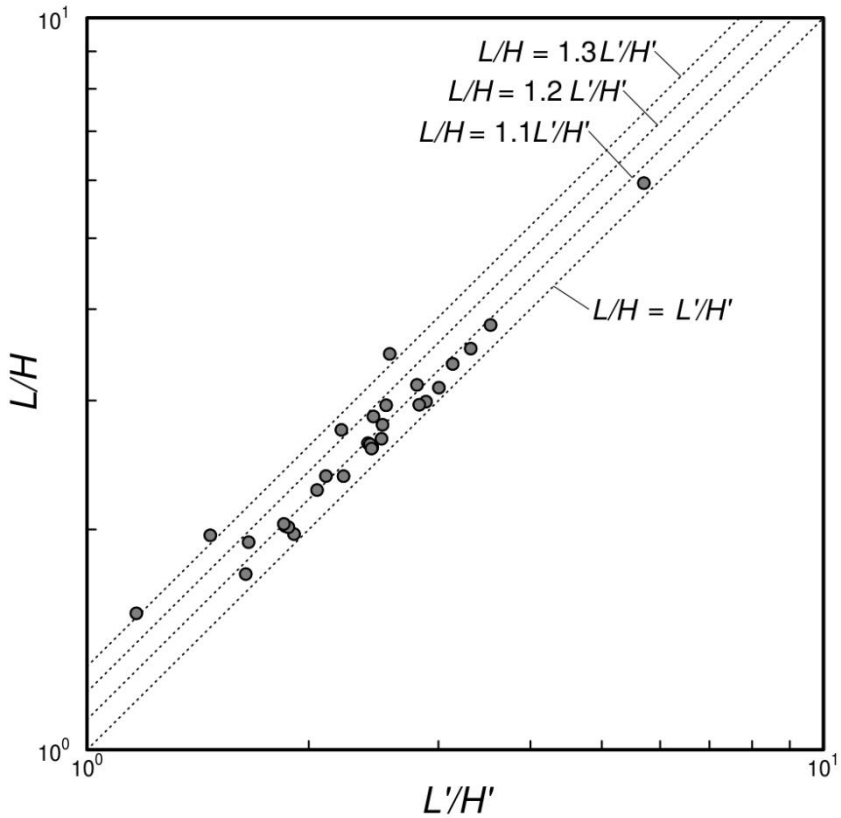

Figure S3. Comparison between *L′/H′* and *L/H*. The dotted lines are assumed for *L/H* = *L′/H′* (i.e., 1:1 agreement between *L′/H′* and *L/H*), *L/H* = 1.1 *L′/H′*, *L/H* = 1.2 *L′/H′*, and *L/H* = 1.3 *L′/H′*.

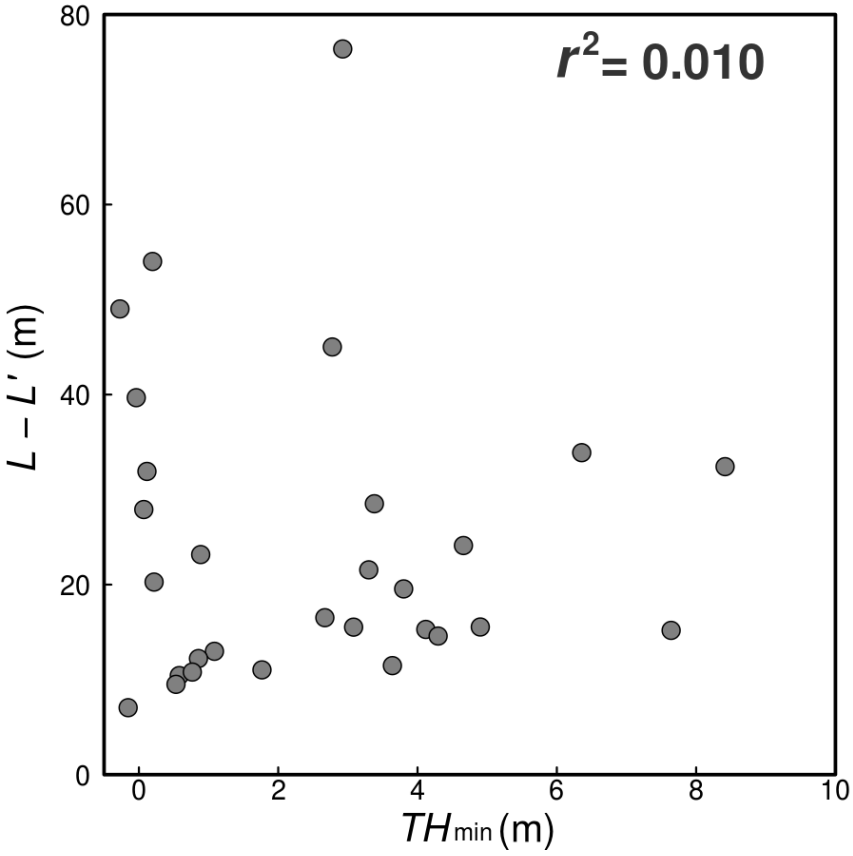

Figure S4. Comparison between TH_{min} before the landslide event and difference between L and L'.

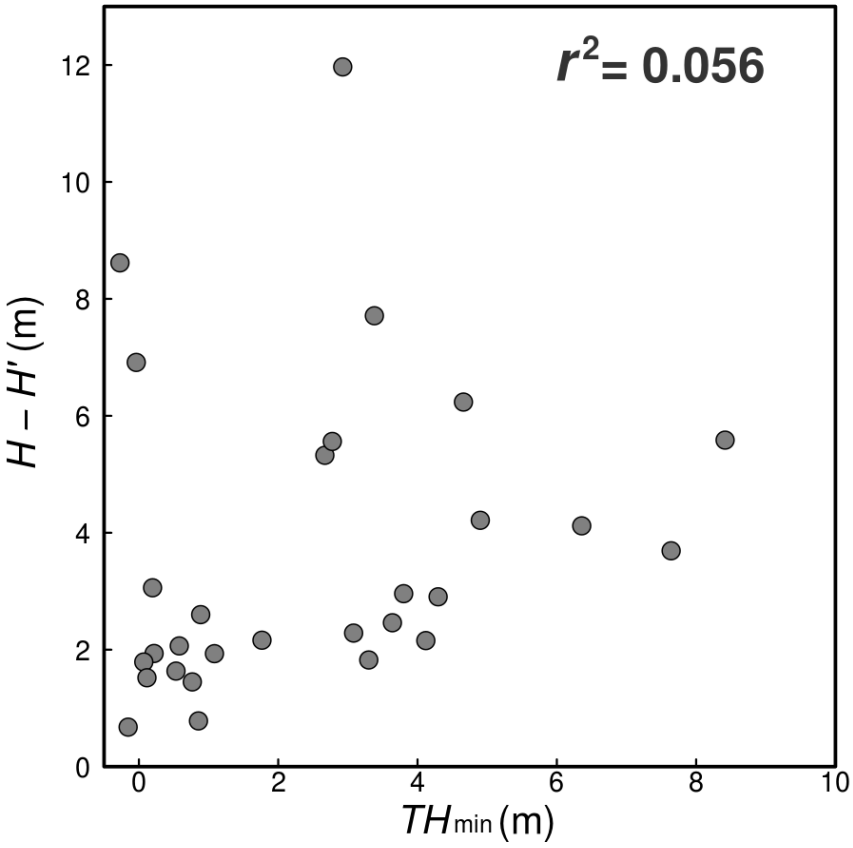

Figure S5. Comparison between TH_{min} before the landslide event and difference between H and H'.